High-Temperature Dielectric Relaxation and Electric Conduction Mechanisms in a LaCoO$_3$-Modified Na$_{0.5}$Bi$_{0.5}$TiO$_3$ System

Surinder Singh,* Anumeet Kaur, Parwinder Kaur, and Lakhwant Singh*
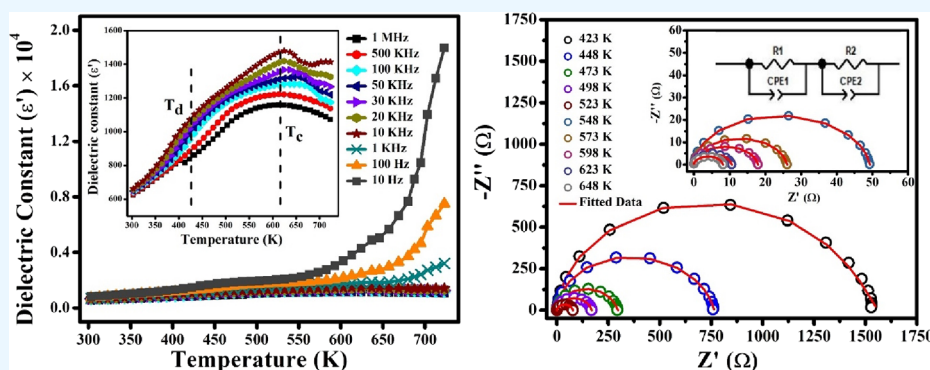
ACCESS | Metrics & More | Article Recommendations | SI Supporting Information

ABSTRACT: This research study examines the high-temperature dielectric relaxation and electric conduction mechanisms in (x)LaCoO$_3$-$(1 − x)$Na$_{0.5}$Bi$_{0.5}$TiO$_3$ samples, where x is 0.05, 0.10, and 0.15. The findings demonstrate that all the samples exhibit two dielectric transitions: first, a frequency-dispersive shoulder at a lower temperature (T_s) around 425−450 K, which is associated with polar nanoregions (PNRs), and second, from ferroelectric to paraelectric transition at the Curie temperature (T_c) approximately between 580 and 650 K. The impedance analysis reveals the negative temperature coefficient of resistance behavior of the specimens. The broad and asymmetric relaxation peaks obtained from modulus spectroscopy demonstrate a wide range of relaxations, suggesting non-Debye-type behavior. Furthermore, the conductivity studies provide insights into understanding the transport phenomena in the samples. The oxygen vacancies resulting from the addition of LaCoO$_3$ into the Na$_{0.5}$Bi$_{0.5}$TiO$_3$ ceramics are responsible for the relaxation and conduction processes, and the charge carrier is doubly ionized oxygen ion vacancies. All samples except for LCNBT10 at 1 kHz exhibit a negative magnetodielectric response.

1. INTRODUCTION

The development of innovative and environmentally sustainable electric energy technologies such as batteries, fuel cells, capacitors, and supercapacitors is of utmost importance in our modern world. These technologies rely heavily on advancements in materials science to achieve greater efficiency in energy storage and conversion.[1−5] Dielectrics, which are materials that do not conduct electricity but play a critical role in electronic devices such as capacitors, actuators, resonators, transistors, and amplifiers, are particularly important in solid-state chemistry.[6]

Ferroelectric materials are a type of dielectric that exhibits intrinsic spontaneous electric polarization below the Curie temperature. These materials have been extensively studied for many years due to their diverse range of applications, including use in random access memory, photovoltaic devices, and magnetic storage.[7−9] Recently, ferroelectric ceramics have become increasingly popular for capacitor applications due to advances in ceramic fabrication and thin-film techniques. Among the various types of ferroelectrics, perovskite oxides with an ABO$_3$ stoichiometry are the most common. These

materials have unique characteristics such as ferroelectric, dielectric, piezoelectric, photoelectric, and conductive properties, which have drawn much attention in the field of functional electrical devices.[10−13] Lead-based ferroelectric ABO$_3$ materials such as PbTiO$_3$ (PTO) have outstanding piezoelectric, pyroelectric, and ferroelectric capabilities, making them widely used in various devices.[14,15] However, the toxicity of lead and its negative impacts on the environment and human health have prompted a shift toward lead-free alternatives.

Sodium bismuth titanate (NBT) ceramics, which belong to the perovskite category, have been extensively studied as a replacement for lead-containing dielectric materials due to their comparable structure to that of lead-based materials.[16,17]
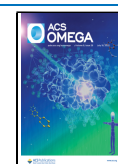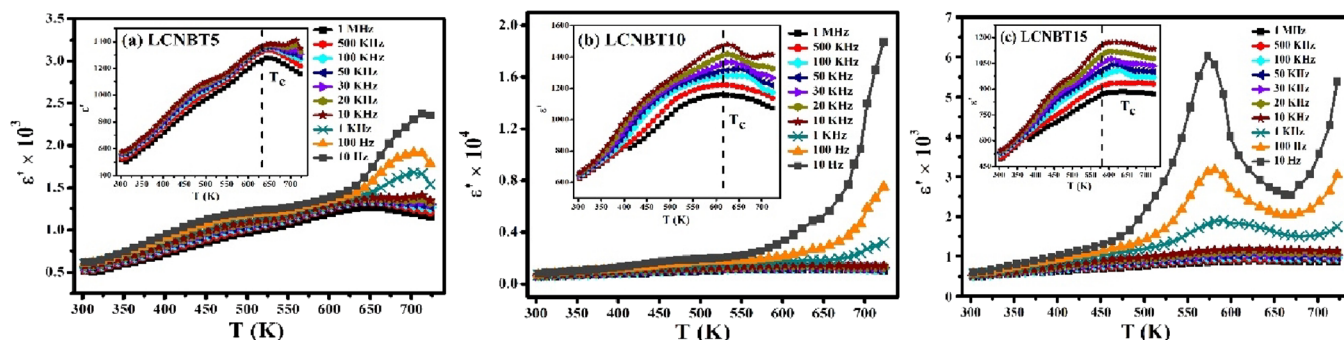
Figure 1. Temperature dependency of the dielectric constant at different frequencies for (a) LCNBT5, (b) LCNBT10, and (c) LCNBT15. Insets show the zoomed-in view for the lower frequencies.

The substitution of the Bi^{3+} ion for the Pb^{2+} ion has been proposed owing to the Bi^{3+} ion's comparable lone-pair electronic $6s^2$ structure.[18] The Bi^{3+} and Na^+ ions have significantly different radii and valence states, and the lone-pair electrons of Bi^{3+} add to the increased disorder.[19] NBT shows a rhombohedral $R3c$ to tetragonal $P4bm$ transition at 400 °C and a tetragonal $P4bm$ to cubic $Pm3m$ phase transition at 500 °C, as confirmed by X-ray diffraction studies.[20,21] Additionally, neutron diffraction studies suggest that the room temperature phase of NBT is monoclinic Cc.[20,22] The superior properties of lead-free NBT, including a high polarization P_r of 38 μC cm^{-2} at room temperature, a high Curie temperature T_c of 320 °C, and a coercive field E_c of 73 kV cm^{-1}, make it an attractive alternative to lead-based ceramics.[23,24]

The conduction process and its structural basis are crucial in understanding the electrical performance of solid dielectrics. A-site or B-site nonstoichiometry in NBT derivations has been found to trigger oxygen ion mobility. Volatilization of Bi^{3+} and Na^+ during the sintering process results in ionic conductivity capability as compensation for oxygen vacancies, allowing a charge balance to be achieved. The weak covalency bonds between Bi and O in pristine NBT with A-site disorder produce significant polarization and strong leakage conductivity.[25] Thus, ionic conductivity is expected in an oxygen-deficient composition, as vacancies can be utilized to hop between surrounding oxygen sites.

Furthermore, NBT materials are nontoxic, lead-free composites, making them an essential component of a cleaner, greener world. To enhance the ionic conductivity of NBT materials, researchers have used first-principles simulations and density functional theory methods to investigate the chemical and phase stability, diffusion processes, defect chemical mechanism, and electrical characteristics of NBT perovskite materials. Doping alternative ions on the A- and/or B-sites of NBT with equivalent ionic radii can improve the structural and electrical characteristics of NBT, with nonstoichiometry at the A-site (Na or Bi) having a significant impact on the electrical conductivity and conductivity mechanism.[26-29]

Magnetoelectric coupling, which describes the connection between the magnetic and electric properties of a material, has attracted considerable attention in recent years. This phenomenon manifests itself as an external magnetic field inducing electric polarization or an external electric field inducing a magnetic moment. Magnetodielectric measurements are often used to assess this coupling, which involves measuring the dielectric constant or capacitance of a material under varying magnetic fields.[30] However, it is important to note that the magnetodielectric response (MDR) can also arise

from factors unrelated to magnetoelectric coupling.[31] Nevertheless, multiferroic composites that exhibit M-E coupling have shown promise in the development of multifunctional devices, with the magnetodielectric response being a particularly intriguing aspect.[32]

In light of these potential applications, there is still ample scope for further study in this field. This study focused on investigating the dielectric relaxation and electrical charge transport characteristics of $LaCoO_3$-doped NBT materials synthesized using the sol–gel process. The samples were characterized for impedance, dielectric, and magnetodielectric properties. In addition, the magnetodielectric properties of these materials were explored, with the aim of assessing their potential for multifunctional device applications.

2. EXPERIMENTAL SECTION

The polycrystalline $LaCoO_3$-doped NBT ceramics ($x LaCoO_3$-$(1-x)Na_{0.5}Bi_{0.5}TiO_3$), with compositions of x = 0.5, 0.10, and 0.15 (abbreviated as LCNBT5, LCNBT10, and LCNBT15, respectively), were synthesized via the sol–gel process, as previously reported.[17] The electrical properties of the samples were characterized using complex impedance and modulus formalism, as well as dielectric, electric modulus, conductivity, and complex impedance spectroscopy. Circular silver electrodes were fabricated on both sides of the sintered pellet using the silver paste, and the measurements were carried out using sandwich geometry.

Impedance analyzers are commonly used in materials science to measure electrical properties such as conductivity and dielectric constant. When studying the temperature-dependent behavior of these properties, it is important to ensure that temperature variation is accurately controlled and monitored. This requires careful consideration of factors such as the heating rate, temperature uniformity, temperature measurement, and thermal insulation. By controlling these factors, accurate and reliable temperature-dependent impedance data can be obtained. The measurements were performed over a broad frequency range (10 Hz to 1 MHz) using a NOVO-CONTROL (Alpha-A) high-performance frequency analyzer at temperatures ranging from 300 to 725 K. The magnetodielectric characteristics were assessed using a high-precision impedance analyzer (Keysight-E4990A) over the frequency range of 100 Hz to 10 kHz at room temperature (RT) under varied static magnetic fields.
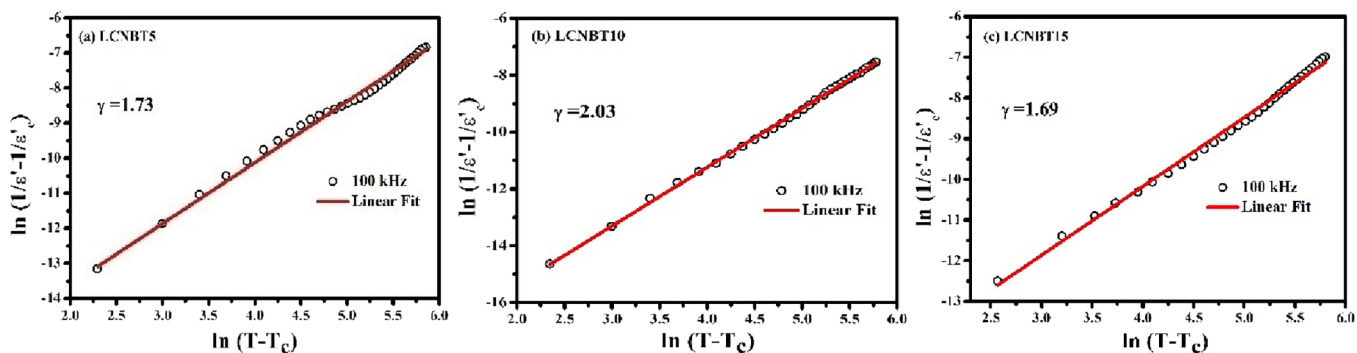
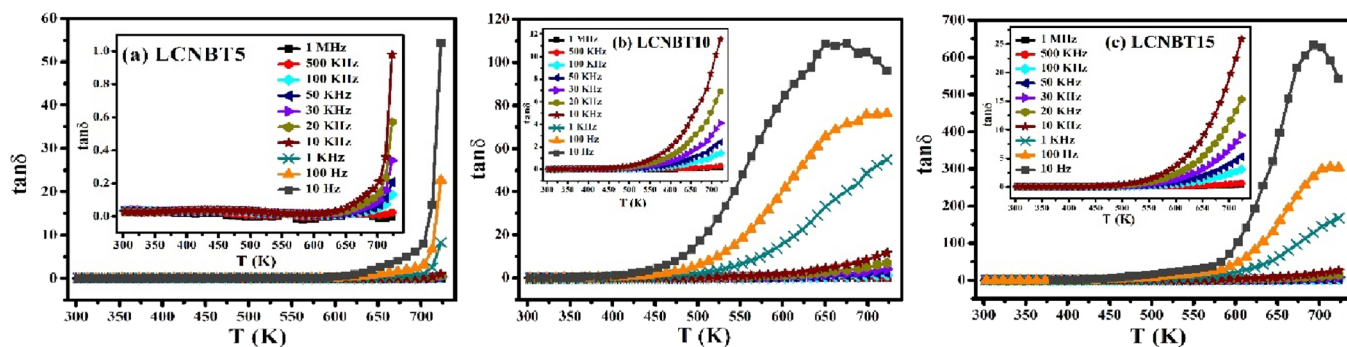**Figure 2.** Degree of diffusivity, γ calculated for (a) LCNBT5, (b) LCNBT10, and (c) LCNBT15 samples.

Figure 3. Temperature dependency of the dielectric loss at different frequencies for (a) LCNBT5, (b) LCNBT10, and (c) LCNBT15 samples. Insets show the zoomed-in view for the lower frequencies.

3. RESULTS AND DISCUSSION

3.1. Dielectric Measurements. The investigation of dielectric behavior and parameters, such as the dielectric constant and loss, in ceramics has become increasingly significant in recent years due to their potential applications in energy storage and ferroelectric industries. The dielectric constant measures the resistance caused by an established electric field, while the emergence of the dielectric tangent loss (tan δ) occurs as the applied electric field increases and polarization falls behind.[33] These dielectric characteristics are primarily determined by the structure and experimental conditions such as frequency and temperature, providing insights into the various polarization processes taking place within the material.

3.1.1. Temperature-Dependent Dielectric Analysis. Figure 1a–c illustrates how the dielectric constant (ε') varies with temperature at different frequencies for LCNBT5, LCNBT10, and LCNBT15. The dielectric constant (ε') has been observed to increase as the temperature rises to Curie temperature, T_c, and then starts decreasing for all the samples. This increment in the dielectric constant is mostly attributed to the rise in charge carrier mobility as the temperature rises, which increases space charge polarization and conductivity. However, above the transition temperature, T_c, the decrease in the dielectric constant is due to an increase in the thermal oscillation of the molecules and an increase in the degree of disorder of dipoles. The values of dielectric constants at low-frequency have been discovered to be greater than those of the higher frequencies. This is because at low frequencies, the dielectric constant values are mostly attributable to dipolar and interfacial polarization, but at higher frequencies, only electronic polarization contributes to dielectric permittivity.[34,35] Furthermore, with increasing temperature and

frequency, ε' improves and becomes more stable.[36] Electronic hopping between Co^{3+} and Co^{2+} ions causes this behavior. Because electron hopping causes electrons to dislocate in the direction of the external electric field and is thermally activated as the temperature rises, polarization is enhanced, and thus, the dielectric constant rises.[37]

Figure 1a–c shows that the LCNBT samples exhibit two distinctive anomalies in dielectric spectra, that is, a frequency-dispersive shoulder at a lower temperature (T_s of ~425 to 450 K) and a diffuse peak at a higher temperature (dielectric maximum temperature, T_c of ~580 to 650 K), demonstrating the unique characteristic of relaxor ferroelectrics. It has been shown for NBT-based materials that the low temperature anomaly is due to thermal evolution of relaxation time distribution or correlation length distribution of polar nanoregions (PNRs). Upon further heating, the PNRs can be transformed reversibly below the temperature of dielectric maximum, Curie temperature (T_c).[38]

With an increment in the applied frequency, the position of the peak at a given temperature (T_c) moves toward a lower temperature, thus showing good ferroelectric relaxor material properties. When Ti is replaced with Co and doping concentrations increase, the T_c value decreases. This shows that the phase transition temperature depends on the content of the $LaCoO_3$ dopant. The values of T_c for LCNBT5, LCNBT10, and LCNBT15 samples are ~645K, 625, and 600 K, respectively. The temperature window for the transition peak is wider than for pure NBT, implying that doped materials have some diffusive characteristic. As a result, Co doping causes the ferroelectric ceramics to become more relaxor-like. On Co substitution, the amplitude of maximum ε' falls by an order of magnitude. On the contrary, the value of ε' rises as the concentration of Co rises. The charge imbalance is
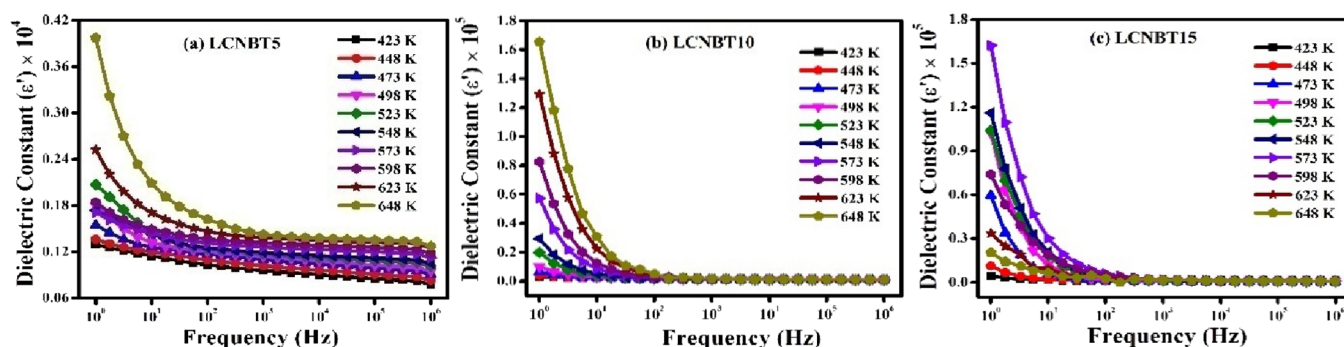
Figure 4. Frequency dependency of the dielectric constant at different temperatures for (a) LCNBT5, (b) LCNBT10, and (c) LCNBT15 samples.

caused by compositional disorder (fluctuation), which results in a higher ε' value.

The modified Curie–Weiss law is utilized to evaluate the order of diffusivity or disorderliness in materials: $(1/\varepsilon_r - 1/\varepsilon_c) = (T - T_c)^\gamma/C$, where γ denotes the diffusivity and C represents the Curie–Weiss constant, whereas ε_r denotes the dielectric constant at temperature T, and ε_c is the maximum value of the dielectric constant at T_c. The slope of $\ln(1/\varepsilon_r - 1/\varepsilon_c)$ with $\ln(T - T_c)$ is used to compute the value of γ as shown in Figure 2a–c for LCNBT5, LCNBT10, and LCNBT15. Diffusivity is usually between 1 and 2. A normal Curie–Weiss law is found in the case of $\gamma = 1$, which reflects a typical ferroelectric–paraelectric phase transition, and $\gamma = 2$, for complete diffusive phase transitions. The degree of diffusivity of the phase transition may be described using the value of γ. For 100 kHz, the computed value was found to be 1.73±0.030, 2.03±0.011, and 1.69 ±0.022 for LCNBT5, LCNBT10, and LCNBT15, respectively, indicating that the phase transition in NBT is a diffuse phase transition (DPT).[39]

At different frequencies, Figure 3a–c displays the temperature dependency of the dielectric loss (tan δ) for LCNBT5, LCNBT10, and LCNBT15 samples. The temperature dependency of the tangent loss investigation reveals that the loss is almost constant for the temperature range below T_c; however, as the T_c is reached, tan δ starts increasing. As a result of the incorporation of Co^{3+} into the Ti^{4+} site, the value of tan δ increases as the concentration of Co increases. This increase in tan δ is most noticeable at high temperatures and low frequencies due to the high value of electrical conductivity. Consequently, the electric dipole motion is maximum at these temperatures, and the mobility of charge carriers is the key mechanism of ionic conductivity in this system.[40] The alkali ion has long been recognized to be an excellent current carrier in ceramics; as a result, these ions play an essential part in the conductivity of NBT ceramics since the Na^+ ions migrate readily when heated, causing an increment in conductivity as the sample temperature rises. The rise in tan δ is slower in the low-temperature area and comparatively faster in the high-temperature region, indicating the existence of undefined imperfections, i.e., oxygen vacancies, as well as the distribution of charge carriers in specimens.[41] For the LCNBT5 sample, the tan δ has a very low value up to 573 K and increases after reaching this temperature; however, the value of tan δ increases after reaching 423 and 473 K, respectively, for LCNBT10 and LCNBT15 samples as can be seen from Figure 3a–c. The highest value of the dielectric constant, in addition to the low value of the dielectric loss of the investigated

compounds, is highly suitable for a variety of device applications.

3.1.2. Frequency-Dependent Dielectric Analysis. The variations in the dielectric constant (ε') with respect to the frequency for various compositions ($x = 0.05, 0.1,$ and 0.15) over a wide temperature range of 423 to 648 K are illustrated in Figure 4a–c. At low frequencies, the dielectric constant exhibits a high value, which gradually decreases as the frequency increases until it reaches a plateau at high frequencies. This can be attributed to the fact that all polarization processes occur predominantly in the low-frequency domain, leading to complete polarization upon the application of an electric field. Furthermore, the accumulation of charges at the interface and the amplification of polarization contribute to the retention of high dielectric constant values in this region. Due to the inertia of the fast-moving ions (dipoles) and the small value of the dielectric constant, the space charge polarization diminishes and becomes negligible as the frequency is increased over 10 kHz.[42] This is according to Koops' theory, which explains that the dielectric constant of a composite system has a large value at low frequencies due to the presence of various polarization processes. These processes contribute to complete polarization in the presence of an electric field, leading to an accumulation of charges at the interface and enhanced polarization. However, as the frequency increases, the fast-moving ions (dipoles) in the composite system are unable to respond quickly enough to the electric field, resulting in a decrease in the dielectric constant. This behavior is attributed to the composite system's heterogeneous conduction mechanism, which gives rise to space charge polarization.[43] As the frequency exceeds 10 kHz, the amount of space charge polarization diminishes, leading to a frequency-independent dielectric constant. On the other hand, electron exchange between Co^{2+} and Co^{3+} ions and Ti^{3+} and Ti^{4+} ions at the octahedral site explains the reduction in the dielectric constant at higher frequencies, which cannot keep up with the rapid changes in the alternating electric field, lowering space charge polarization and therefore the dielectric constant.[44]

Free dipoles oscillating in a similar field are connected to the modified Debye rule. Measurements and dipole relaxation time follow the field at lower frequencies; however, the dipoles do not follow the oscillatory field at higher frequencies. The significant dielectric constant value may be explained using the Maxwell–Wagner model and Koop's two-layer model at low frequencies and high temperatures.[45,46] According to this model, a dielectric medium must be composed of strongly conducting grains with poorly conducting grain boundaries.
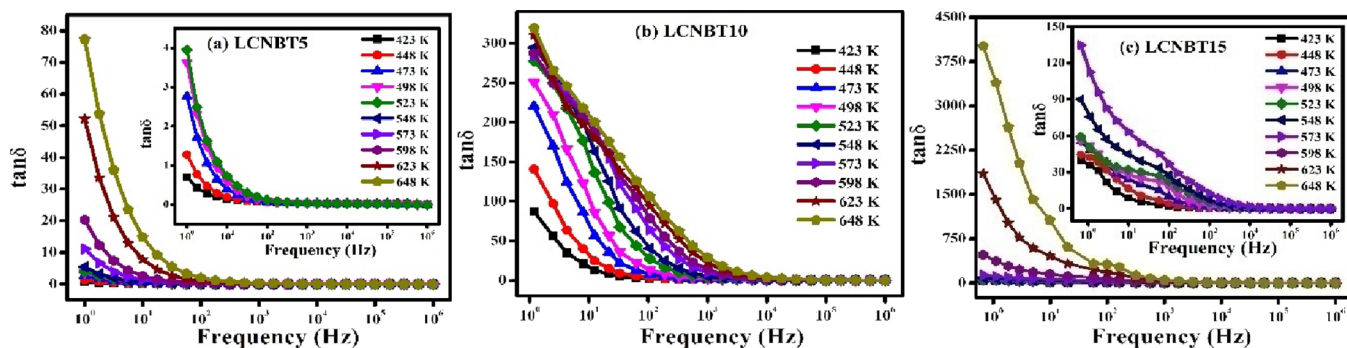
Figure 5. Frequency dependency of the dielectric loss at different temperatures of (a) LCNBT5, (b) LCNBT10, and (c) LCNBT15 samples. Insets show the zoomed-in view for the lower temperatures.
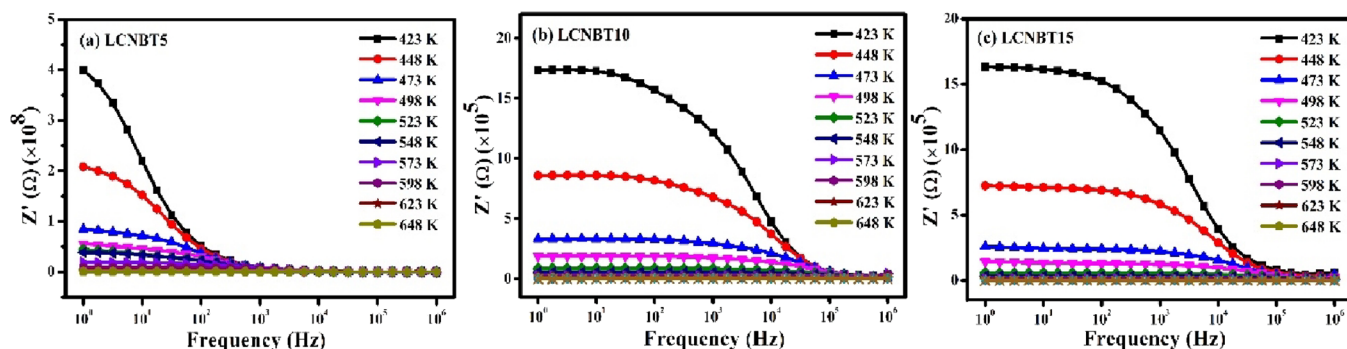

Figure 6. Variation of the real part of complex impedance, Z', as a function of the frequency (1 Hz−1 MHz) at different temperatures for (a) LCNBT5, (b) LCNBT10, and (c) LCNBT15.

Grain boundaries, on the other hand, tend to be quite impactful in the low-frequency range, while grains appear to be more efficient at higher frequencies. Moving the charge carriers at low frequencies requires more energy. The charge carriers concentrate near the grain boundary because of the high resistance, giving rise to a high dielectric constant in this region. In the high-frequency band, the energy required to transport the charge carriers is lower because of the low resistance supplied by the grains. As a result, at high frequencies, the dielectric constant is comparatively low.[47]

The dielectric loss factor (tan δ) is a generic description of the energy loss in a dielectric system. The tangent loss (dielectric loss) acts similarly to the dielectric constant (ε') and exhibits dispersion at low frequencies, as displayed in Figure 5a−c. With the introduction of an ac electric field, the tan δ values drop, and at higher frequencies, they display frequency-independent behavior. This trend may be based on the argument that in the low-frequency region, in which weakly conducting grain boundaries are much more efficacious, more energy is required for electron hopping between Co^{2+} and Co^{3+} ions, leading to larger losses. However, the high-frequency area corresponds to the strongly conducting grain, and electron interaction between Co^{2+} and Co^{3+} results in a little energy dissipation.[48] Furthermore, when the temperature rises, so does the value of the loss tangent. When the temperature is low, the rate of rise of tan δ is sluggish, but when the temperature is high, the rate of increase is significantly faster. At low frequencies, charge carriers passing across the grain boundary lose a significant amount of energy, and tan δ has a high value in this area, but resistance is low in the high-frequency zone. The tangent loss, on the other hand, denotes the amount of energy expended by the applied field to

align the dipole. The grain size, oxygen vacancies, and DC conductivities are all factors that affect the tangent loss.[49]

3.2. Complex Impedance Spectroscopy (CIS). To analyze the dielectric spectra, various formalisms such as the complex electric modulus M^* and complex impedance Z^* have been explored.[50] The M^* formalism is useful when localized relaxation dominates capacitive and/or resistive analysis, whereas the Z^* formalism is preferred when long-range conduction dominates. The complex impedance can be calculated using eq 1.[51]

$$Z^* = Z' - iZ'' = \frac{1}{i\omega\varepsilon_0\varepsilon^*} \tag{1}$$

where Z' and Z'' denote the real and imaginary parts of complex impedance, respectively, ε_0 represents the vacuum permittivity, and ε^* denotes the complex dielectric permittivity.

The use of the Z^* formalism enables the direct separation of bulk and bulk/electrode interface phenomena.[52] In addition, CIS is employed to investigate the ionic conductivity of ceramics, and the shape of the impedance spectra provides information about the electrode polarization and the type of charge carrier (i.e., electrons or ions).[53] CIS can also be utilized to study the conduction process and quantify electrical conductivity by distinguishing dielectric responses in ceramics based on relaxation time.[54]

3.2.1. Frequency-Dependent Analysis of Real and Imaginary Parts of Impedance (Z′ and Z″) at Different Temperatures. The frequency-dependent real part of complex impedance (Z') of LCNBT samples calculated at various temperatures is depicted in Figure 6a−c. With raising f to a certain point, Z' lowers noticeably, accompanied by a slower
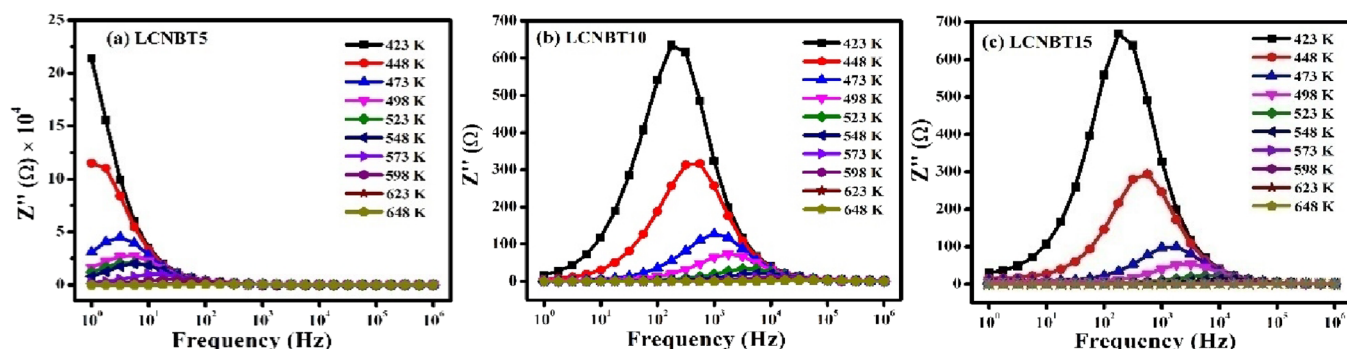
Figure 7. Variation of the imaginary part of impedance, Z'', as a function of the frequency (1 Hz–1 MHz) at different temperatures for (a) LCNBT5, (b) LCNBT10, and (c) LCNBT15.
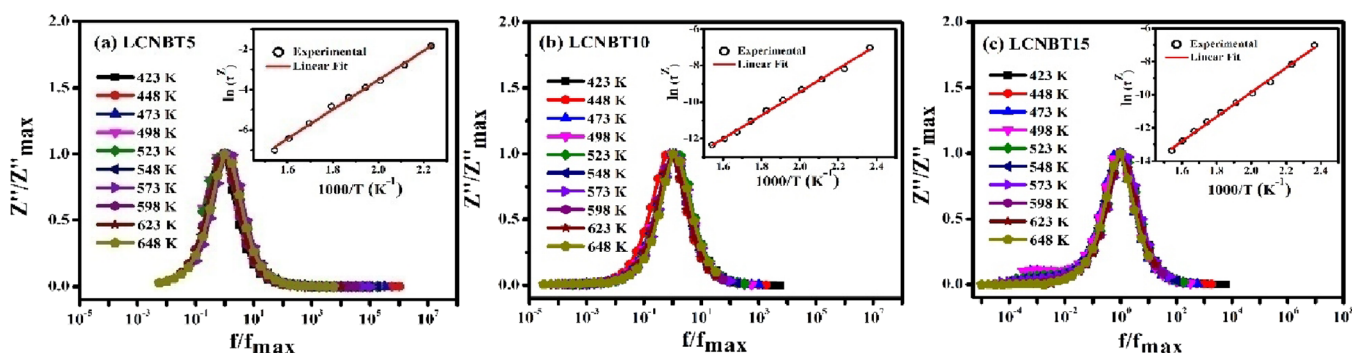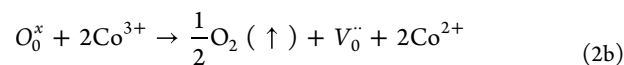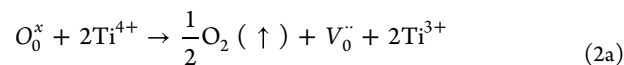

Figure 8. Scaling behavior of Z'' spectra for (a) LCNBT5, (b) LCNBT10, and (c) LCNBT15. Insets show the Arrhenius fit to the relaxation time.

frequency response in a linear scale. With decreasing f, the observed switching mechanism below 1–10 kHz might be attributed to a transition from short-range hopping to vacancy-assisted long-range ionic motion.[55] At high temperatures, however, the values of Z' become almost zero and are temperature-independent, which might be owing to the release of space charge.[56] The observed drop in Z' with rising f might be due to polaronic-type electron hopping over a potential barrier between two neighboring localized sites with varying oxidation states (e.g., Ti^{4+}/Ti^{3+} and Co^{3+}/Co^{2+}) in the high-f range. Long-range frequency responses of heavy charge carrier units like ions/vacancies are improbable at this stage; therefore, another source might be extremely short-range vacancy-assisted back-and-forth ionic hopping. As long-range translational procedures for dipoles with higher inertia are predicted to be slowly initiated with a declining frequency, a rapid spike in Z' below 1 kHz signifies the start of the interfacial polarization process.

In Figure 6, a significant decline in Z' with increasing measurement temperature, at low f, is a representation of negative temperature coefficient of resistance (NTCR) behavior, which is attributed to many processes. At high temperatures, the accumulated charge species (polaronic and vacancy types) may be thermally activated at the crystal/grain interfaces and overcome the interface barriers, enhancing conductivity. Furthermore, the ionization of oxygen vacancies ($V_0^{..}$) at T_{sint}, in titanates, is attributed to the production of polaronic charge species, which produces conduction electrons that are absorbed by Ti^{4+} and Co^{3+} ions, resulting in Ti^{3+} and Co^{2+} ions, consequently forming polaronic hopping sites,[57] as shown below:

$$O_0^x + 2Ti^{4+} \rightarrow \frac{1}{2}O_2 (\uparrow) + V_0^{..} + 2Ti^{3+} \tag{2a}$$

$$O_0^x + 2Co^{3+} \rightarrow \frac{1}{2}O_2 (\uparrow) + V_0^{..} + 2Co^{2+} \tag{2b}$$

As a result, polaronic conduction entails the hopping of Co and Ti 3d electrons across neighboring sites.[58]

The relaxation process of the investigated compounds is examined using a Bode plot of the imaginary part of impedance (Z'' vs frequency) for LCNBT5, LCNBT10, and LCNBT15 specimens at various temperatures (see Figure 7a–c). The graph was plotted at various temperatures to show the materials' relaxation peak, and for all the samples, the relaxation peak is shown to be temperature-dependent. The spectra show well-defined broad and asymmetric relaxation peaks, showing a wide range of relaxation durations, indicating non-Debye-type behavior. A broad peak is detected in all of the synthesized samples, and this maximum frequency is known as the relaxation frequency (f_{max}). As the temperature rises, the observed peak shifts slightly to the higher-frequency side, and the peak's height steadily diminishes. This phenomenon can be explained by the fact that the rate of electron hopping increases as the temperature rises. As the temperature rises, the hopping electron has a shorter relaxation time and is incapable to match the frequency of the alternating field, resulting in a decrease in polarization at higher frequencies.[59] Furthermore, all of the Z'' overlap in the high-frequency area. This indicates that space charge polarization persists at lower frequencies but that it is completely ineffective at higher frequencies.[60−62] The decreasing behavior with increasing the temperature facilitates the thermally activated electron hopping mechanism, which thus leads to conduction in these materials at higher temperatures.
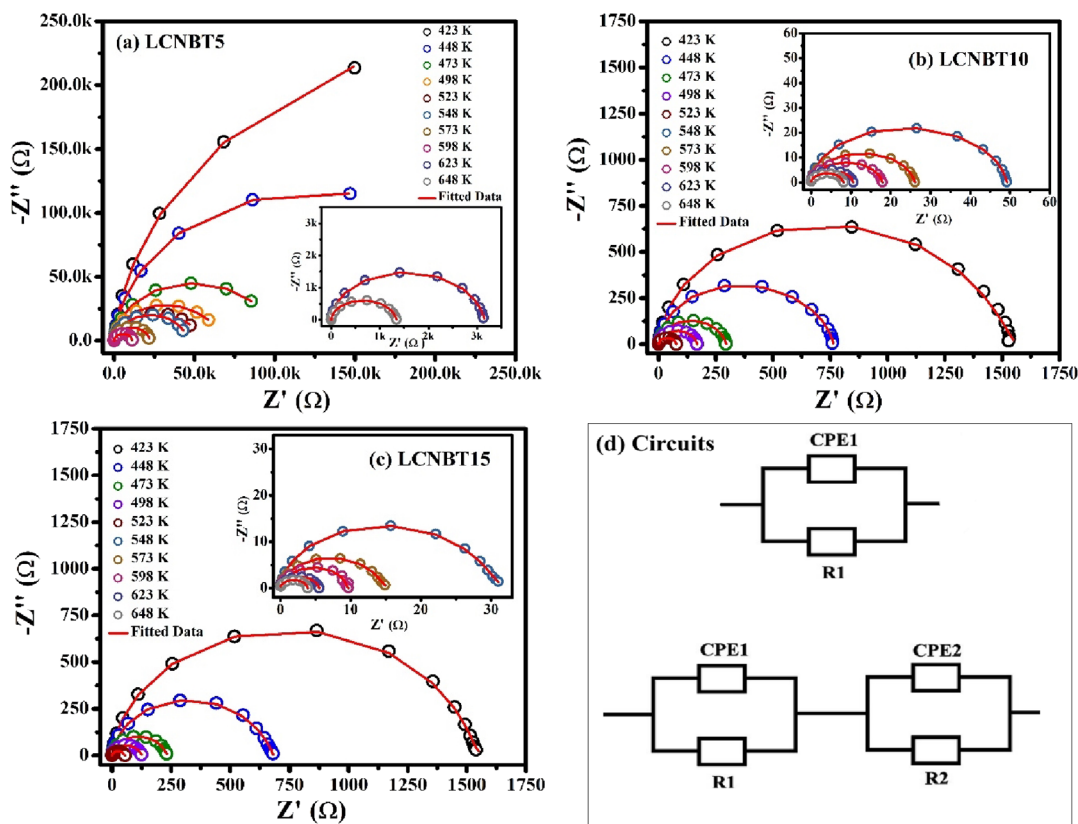
Figure 9. Cole−Cole plots of Z' vs Z'' for (a) LCNBT5, (b) LCNBT10, and (c) LCNBT15 samples at different temperatures and (d) equivalent circuits used R1-CPE1 for LCNBT5 and R1-CPE1−R2-CPE2 for LCNBT10 and LCNBT15.

The Arrhenius relation is also satisfied by the reciprocal dependency of relaxation time on temperature as follows:

$$\tau^z = \tau_0^z \exp\left(\frac{-E^{(z)}}{k_B T}\right) \tag{3}$$

where τ_o is the pre-exponential factor, E_a denotes the activation energy (in eV), T represents the temperature (in Kelvin), k_B is the Boltzmann constant, and the relaxation frequency (f_{max}) corresponds to the maximum value of Z''. The value of τ can be calculated (from the inset of Figure 8a−c) as follows:

$$\tau^z = \frac{1}{\omega_{max}} = \frac{1}{2\pi f_{max}^{(z)}} \tag{4}$$

The activation energy (E_a) values for LCNBT5, LCNBT10, and LCNBT15 determined using eq 3 are 0.63, 0.55, and 0.64 eV, respectively.

At various temperatures, Figure 8a−c illustrates the scaling pattern of normalized complex impedance (Z''/Z''_{max}) with the logarithm of the normalized frequency ($\log(f/f_{max})$), where f_{max} is the frequency corresponding to the highest value of Z'' (Z''_{max}) for LCNBT5, LCNBT10, and LCNBT15. All of the curves in each sample are well-overlapped, implying that the same relaxation process occurs in the composite at different temperatures.[63]

3.2.2. Cole−Cole Plots. Impedance spectroscopy commonly employs Cole−Cole plots to analyze the complex impedance of materials. These plots display the relationship between the real part (Z') and imaginary part (Z'') of the impedance. The Cole−Cole plot is especially useful for investigating the electrical properties of materials that display non-Debye behavior, including some ceramics, biological tissues, and polymers. The deviation of the semicircle from a perfect circle indicates the existence of multiple relaxation processes or nonuniform distributions of relaxation times. In general, the Cole−Cole plot provides valuable insight into the molecular structure and dynamics of a material and can be used to examine its dielectric properties.

The Cole−Cole plots with equivalent circuit components of the examined systems LCNBT5, LCNBT10, and LCNBT15 at selected temperatures in the frequency range of 10^1−10^7 Hz are displayed in Figure 9a−d. In polycrystalline ceramics, the bulk, grain boundary, and electrode interface behaviors may all be attributed to the three independent components in CIS. The Cole−Cole plot usually shows a series of semicircular arcs corresponding to the contribution of each particular component. The resistance of the associated effect is calculated by intercepting the semicircular arc along the Z' axis. To describe the material's transport characteristics, these experimental results are usually fitted with a corresponding circuit composed of fundamental electric components such as resistance (R), capacitance (C), and constant phase elements (Q) arranged in a parallel combination.[64−66] The observed Cole−Cole plots are used to resolve the dielectric relaxation mechanism caused by the grain and grain boundary.[67] The impedance data were fitted with an appropriate circuit using EIS software.[68] This circuit is composed of a combination of resistance (R) and a constant phase element (CPE) (Q). The impedance of the CPE is expressed by the equation $Z_{CPE} = 1/(j\omega)^\alpha Q$ that deviates from the ideal Debye-type model. Here, Q is equal to the numeral value of $1/|Z|$ at $\omega = 1$ rad s^{-1}, and α denotes the phase of the elements, which gives the degree of

Table 1. The Values of the Resistances and Constant Phase Elements at Various Temperatures for LCNBT5, LCNBT10, and LCNBT15 Samples Estimated from Complex Impedance Data

| temp. (K)	LCNBT5		LCNBT10				LCNBT15			
	R1	CPE1	R1	CPE1	R2	CPE2	R1	CPE1	R2	CPE2
423	471,320	8.48×10^{-8}	1163	1.22×10^{-7}	374	1.77×10^{-6}	1028	2.29×10^{-7}	501.7	2.14×10^{-7}
448	240,590	8.79×10^{-8}	470.7	1.20×10^{-7}	290.9	1.07×10^{-6}	402.3	1.56×10^{-7}	272.1	5.38×10^{-7}
473	95,115	9.12×10^{-8}	172.5	1.21×10^{-7}	122.2	8.92×10^{-7}	225	1.39×10^{-7}	28.74	1.16×10^{-8}
498	60,608	9.40×10^{-8}	103.1	1.24×10^{-7}	64.73	8.32×10^{-7}	119.9	1.38×10^{-7}	19.26	1.15×10^{-8}
523	47,194	9.95×10^{-8}	50.16	1.23×10^{-7}	27.06	8.04×10^{-7}	49.76	1.37×10^{-7}	5.58	2.63×10^{-8}
548	42,977	9.49×10^{-8}	30.83	1.24×10^{-7}	18.33	6.98×10^{-7}	28.88	1.39×10^{-7}	3.57	3.32×10^{-8}
573	21,509	9.23×10^{-8}	13.2	1.26×10^{-7}	12.83	4.59×10^{-7}	13.9	1.36×10^{-7}	1.649	5.45×10^{-8}
598	10,937	9.34×10^{-8}	9.205	1.23×10^{-7}	8.66	4.46×10^{-7}	8.52	1.75×10^{-7}	1.115	5.26×10^{-8}
623	3101	9.73×10^{-8}	5.845	1.15×10^{-7}	4.71	3.52×10^{-7}	3.57	1.06×10^{-7}	1.957	3.31×10^{-8}
648	1319	1.05×10^{-7}	4.916	1.07×10^{-7}	3.13	2.18×10^{-7}	2.84	7.58×10^{-7}	1.053	2.54×10^{-8}
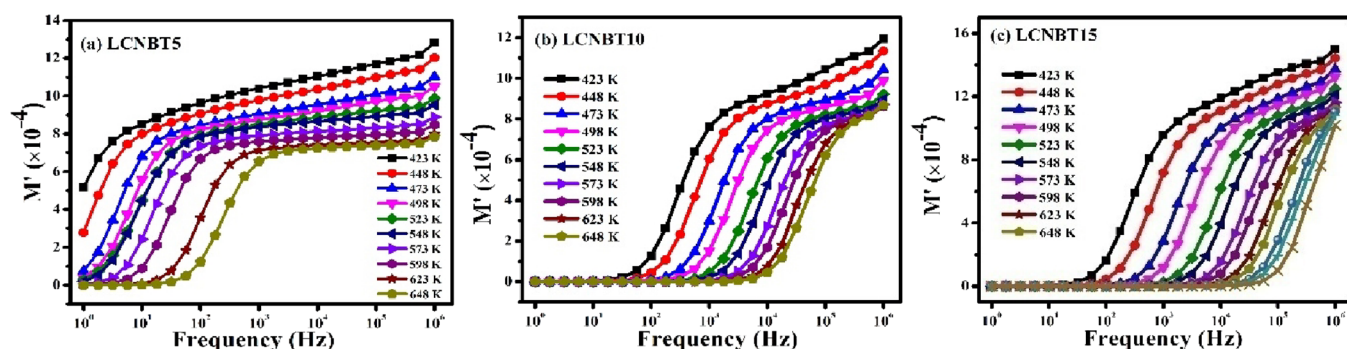
Figure 10. Frequency dependence of the real part of the electric modulus, M', at different temperatures for (a) LCNBT5, (b) LCNBT10, and (c) LCNBT15 ceramics.
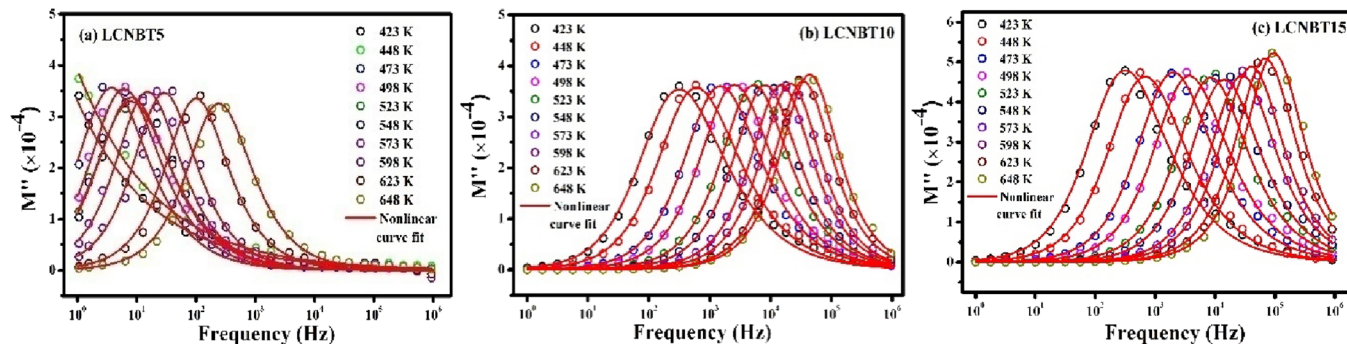

Figure 11. Frequency dependence of the imaginary part of the electric modulus, M'', at different temperatures for (a) LCNBT5, (b) LCNBT10, and (c) LCNBT15 ceramics.

deviation with respect to the pure capacitor. When the CPE is set to $\alpha = 0$, it acts as a pure resistor, and when it is set to $\alpha = 1$, it acts as a pure capacitor.

In our experimental investigation, we found a single semicircular arc with the center placed below the horizontal axis in the Cole−Cole plots corresponding to the LCNBT5 sample. The experimental impedance data of the LCNBT5 sample at various temperatures are fitted with a single R1-CPE1 circuit, as shown in Figure 9d, suggesting that only the grain effect contributes to the polarization and other electrical characteristics of the materials in the temperature range discussed. For LCNBT10 and LCNBT15 samples, poorly resolved semicircles originate in the Cole−Cole plot, which is fitted with a single R1-CPE1−R2-CPE2 circuit, demonstrating the grain and grain boundary effect contribution at all temperatures. As the temperature rises, the diameter of the

semicircle reduces. It simply means that conductivity increases as temperature rises, symbolizing the materials' characteristic negative temperature coefficient of resistance (NTCR) behavior. The fact that the center of the semicircle is placed below the actual impedance (Z') axis suggests that ion relaxation is not of the Debye type.[69] The high degree of agreement between the data and the simulation observations authenticates that the chosen equivalent circuit is a good fit. The analogous circuit model's parameters acquired by fitting the curves of Figure 9 are summarized in Table 1.

3.3. Electric Modulus Analysis. Electrical modulus spectroscopy is a method for determining the electrical characteristics of a prepared sample and examining the impact of different relaxation times (i.e., unrecognized or superimposed effects in the CIS method). The electrical modulus study is employed to estimate (i) electrode polarization, (ii)
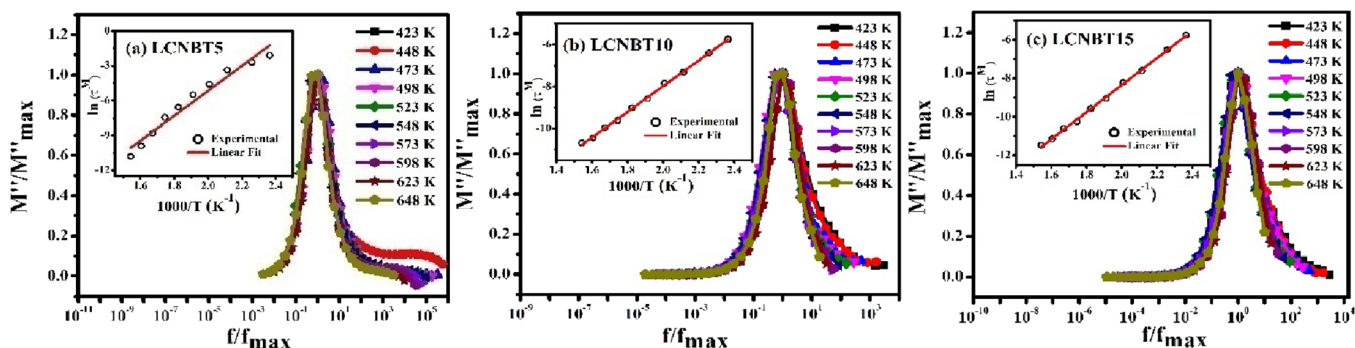
Figure 12. Scaling behavior of M'' spectra for (a) LCNBT5, (b) LCNBT10, and (c) LCNBT15 ceramics. Insets show the Arrhenius fit to the relaxation time.

electrical conductivity, (iii) relaxation time, (iv) grain boundary conduction effect, and (v) bulk characteristics of the synthesized sample.[70]

Figure 10a–c shows how M' varies with the frequency for LCNBT5, LCNBT10, and LCNBT15 samples across a large temperature range (423 to 648 K). The real part of the modulus spectrum (M') of all ceramics follows a pattern in which M' tends to zero in the lower-frequency range, displays continuous dispersion shifting in the mid-frequency band, and reveals plateau-type behavior in the higher-frequency zone. This graph depicts the propensity for all temperatures to saturate at a maximum asymptotic value (i.e., $M_\infty = 1/\varepsilon_\infty$). The shift from low to high values of M' is seen as a sigmoidal shape curve. This characteristic behavior is due to poor electrode polarization at lower frequencies, short-range and long-range mobility of charge carriers in mid-frequencies, and frequency-independent electrical conduction in higher frequencies.[71] As the frequency rises, there is a dispersion, and it coincides at higher frequencies. The major cause for the shift in the value of M' is the progress of short-range charge carriers and non-Debye conduction mechanisms. To provide a constant electric field, the charge movement may be estimated by an inadequate restoring force.[72]

The Bode plot, which shows the fluctuation of the imaginary part of the modulus (M'') with the frequency modulus, is used to investigate the relaxation process. Figure 11a–c depicts the fluctuation of M'' as a function of the frequency for LCNBT5, LCNBT10, and LCNBT15 specimens at different temperatures.

With an increment in temperature, the intensity of the peak reduces, then grows, and also shifts consistently to the higher-frequency side, signifying that dielectric relaxation is thermally triggered, where charge carrier hopping is prevalent[73] and M'' refers to the maximum value for all compositions at a specific frequency known as the relaxation frequency. When the requirement $2f_{max}RC = 1$ is met, the peak in the M'' vs frequency plot is discovered. Furthermore, when the temperature rises, the peak shifts forward, implying that the relaxation time shortens. The relaxation time is mainly caused by segmental motion and dipole orientation, which is aided by the temperature rise.[53] In Figure 11a–c, all of the samples have a similar peak, but at a given temperature, the peak moves toward a higher frequency as the LaCoO₃ concentration increases. Also, the peak frequency of the imaginary part of the electric modulus, M'', moves to the high-frequency zone. This process is more prominent at higher frequencies because the relaxation time of the dielectric constant is temperature-dependent. As the temperature rises, this peak shifts to a

higher-frequency region, implying that in a thermally activated process, the charge carrier hopping mechanism takes precedence naturally at higher temperatures. The broad M'' peaks and asymmetric structure of the curve may be explained as a result of relaxation time distribution and departure from ideal Debye-type behavior.[74] Below and above M''_{max}, two relaxation regions may be seen. The DC conductivity results from the continuous hopping process, in which the charge carriers are movable over extended distances and can be linked to the section on the left side of the peak (low frequency). Moreover, the relaxation polarization system is related to the right side of the peak (high-frequency side), which illustrates the range of frequencies where the ions are spatially limited to their potential wells and can only move short distances within them.[75] As a result, as the frequency rises, the peak frequency represents a shift from long- to short-range mobility.

The examination of relaxation parameters acquired using the Arrhenius law (eq 5) can help to better understand the physical nature of the apparent relaxation:

$$\tau^{(M)} = \tau_0^{(M)} \exp\left(\frac{E^{(M)}}{k_B T}\right) \tag{5}$$

where $\tau_0^{(M)}$ is the pre-exponent factor, $E^{(M)}$ is the activation energy, k_B is the Boltzmann constant, and T denotes the temperature in absolute terms.

The Arrhenius plots for the system under consideration are displayed in the inset of Figure 12a–c. The value of $E^{(M)}$ is obtained using the slope of the linear fit of $\ln(\tau^{(M)})$ versus $10^3 T^{-1}$, which is 0.67, 0.53, and 0.61 eV for the LCNBT5, LCNBT10, and LCNBT15 materials, respectively. M'' was presented in scaled coordinates, i.e., M''/M''_{max} as a function of $\log(f/f_{max})$, to evaluate the temperature dependency of the distribution of relaxation time. The resulting curve is referred to as a master electric modulus curve, and it is further utilized to explain the dielectric processes in the material. The curves in Figure 12a–c all converge to a single master curve, indicating that the relaxation time distribution is temperature-independent. This means that the conduction process is still the same and that the ion transport process is the same as well. As a result, the ion hopping motion might be accountable for the relaxation.[53] However, at higher frequencies, there is non-overlapping of temperature curves. This is because the M'' peak is asymmetric on the higher-frequency side, indicating that the samples have components both from long-range conductivity and nonexponential localized conductivity relaxation.[76]
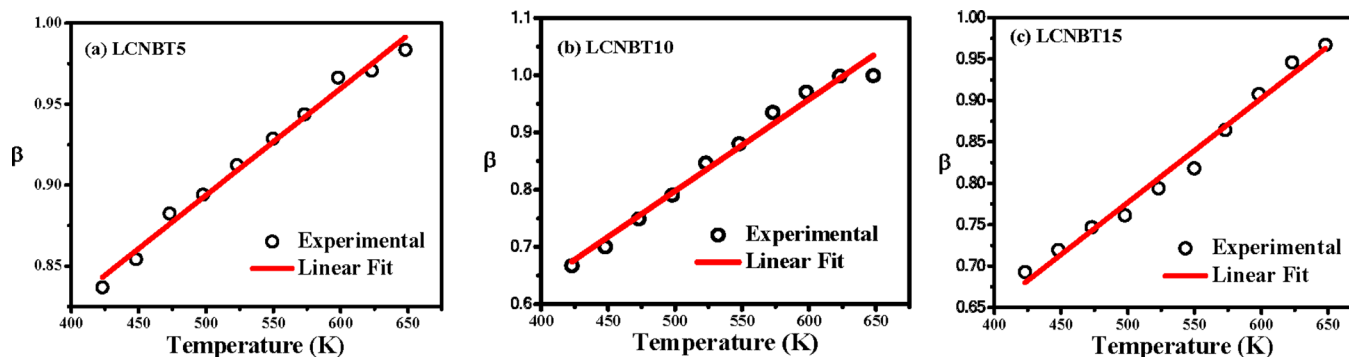
Figure 13. Variation of the relaxation parameter, β, as a function of temperature for (a) LCNBT5, (b) LCNBT10, and (c) LCNBT15.
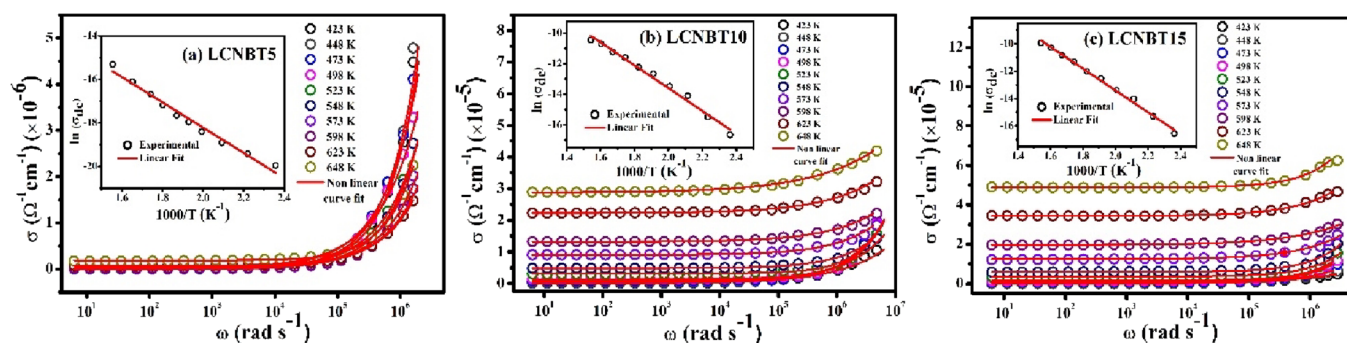

Figure 14. Frequency dependence of ac conductivity in (a) LCNBT5, (b) LCNBT10, and (c) LCNBT15 ceramics. Insets show the Arrhenius fit to the dc conductivity.

The electric modulus behavior of current samples is investigated using Bergman's[77] technique, which defines the imaginary part of the electric modulus as

$$M'' = \frac{M''_{max}}{(1-\beta) + \frac{\beta}{1+\beta}\left[\beta\left(\frac{\omega_{max}}{\omega}\right) + \left(\frac{\omega}{\omega_{max}}\right)^{\beta}\right]} \quad (6)$$

where M''_{max} denotes the maximum value of M'', ω_{max} represents the corresponding maximum angular frequency, and β is the relaxation parameter that characterizes the relaxation time distribution. The value of β reflects the relaxation divergence from Debye-type relaxation (β =1) and is in the range of 0−1. The theoretical fits of the aforementioned equation to M'' experimental findings for LCNBT5, LCNBT10, and LCNBT15 specimens are depicted in Figure 11a−c. The data demonstrate that the acquired outcomes are well-suited to the model (indicated by the red solid line). For all the samples, the values of β so obtained by fitting are enhanced as the temperature rises. The variance of β for all the samples as a function of temperature is displayed in Figure 13, and it is less than 1 for all the samples, suggesting that the relaxation mechanism is not of the Debye form. Furthermore, the values of β decrease with an increase in the $LaCoO_3$ concentration, indicating that adding $LaCoO_3$ to NBT leads the samples to behave more Debye-like. The temperature independence of the values has been revealed, implying that the relaxation time distribution is likewise temperature-independent.

3.4. Electrical Conductivity Formalism. The understanding of the electrical conduction process contributes to studying the dynamics of charge carriers, the effects of the field and temperature on charge motion, and the transport properties of materials. As the ac conductivity is frequency-dependent, it is beneficial in gaining better knowledge of the electrical conductivity of a substance. The relationship between ac conductivity and frequency provides insights into the dynamics of charge carriers. The evaluation of ac conductivity is done using dielectric parameters and an empirical formula as follows:

$$\sigma_{ac} = \omega\varepsilon_r\varepsilon_0 \tan\delta \quad (7)$$

where σ_{ac} denotes the ac conductivity, ω is equal to $2\pi f$ and known as the angular frequency, and ε_0 represents the permittivity of free space, whereas ε_r and $\tan\delta$ are the symbols used to denote the dielectric constant (relative permittivity) and the dielectric loss, respectively. Figure 14a−c shows logarithmic graphs of the change in the conductivity against the frequency for the compounds LCNBT5, LCNBT10, and LCNBT15 throughout a frequency range of 1 Hz−1 MHz and at a temperature range of 448−623 K. Furthermore, all of the composites have two conductivity areas. The conductivity in the first zone (the plateau region) is essentially constant in the low-frequency range, whereas the conductivity in the second region (the dispersion region) is frequency-dependent in the high-frequency range and obeys the power law. The frequency independence of ac conductivity in the low-frequency zone is related to the plateau area, which provides the dc conductivity σ_{dc}. This dc conductivity is attributed to the bulk conductivity of the specimen and occurs as a result of charge carrier hopping from one local state to another.[78] Conductivity increases linearly with the frequency in the high-frequency domain (dispersion area), and the charge carriers have greater mobility.[79]

As the temperature rises, conductivity rises, showing NTCR behavior in the samples, as displayed in Figure 14a−c. The disordering of cations between space charges and neighboring

Table 2. The Fitted Parameters σ_{dc}, n, A, and R^2 at Different Temperatures for LCNBT5, LCNBT10, and LCNBT15 Samples

composition of the sample	temp. (K)	σ_{dc} (Ω^{-1} cm^{-1})	n	A	R^2 (%)
LCNBT5	423	9.78617×10^{-7}	0.94654	1.11254×10^{-11}	99.99
	448	1.42648×10^{-6}	0.91725	1.48592×10^{-11}	99.97
	473	2.02751×10^{-6}	0.88812	5.26267×10^{-11}	99.56
	498	2.88633×10^{-6}	0.83685	1.25861×10^{-10}	99.46
	523	3.91293×10^{-6}	0.8176	5.19308×10^{-11}	99.81
	548	4.81064×10^{-6}	0.7765	1.71885×10^{-11}	99.89
	573	6.75185×10^{-6}	0.75282	3.46002×10^{-11}	99.66
	598	9.49133×10^{-6}	0.7085	3.64667×10^{-11}	99.52
	623	1.41661×10^{-5}	0.69638	2.11896×10^{-11}	99.97
	648	2.44826×10^{-5}	0.65263	4.03547×10^{-12}	99.89
LCNBT10	423	5.77828×10^{-8}	0.92107	2.6706×10^{-9}	99.97
	448	1.86485×10^{-7}	0.80627	1.24372×10^{-9}	99.98
	473	7.48893×10^{-7}	0.76207	1.25879×10^{-10}	99.82
	498	1.3877×10^{-6}	0.70027	5.88825×10^{-11}	99.75
	523	3.16455×10^{-6}	0.62727	9.51456×10^{-12}	99.84
	548	4.84454×10^{-6}	0.59996	2.14936×10^{-10}	99.62
	573	9.09387×10^{-6}	0.53673	6.43762×10^{-10}	99.39
	598	1.31834×10^{-5}	0.52921	2.49561×10^{-9}	99.67
	623	2.2294×10^{-5}	0.49533	5.25394×10^{-9}	99.41
	648	2.87253×10^{-5}	0.40142	2.9001×10^{-8}	99.74
LCNBT15	423	6.41896×10^{-8}	0.85519	1.72654×10^{-9}	99.66
	448	2.29462×10^{-7}	0.83842	7.05779×10^{-10}	99.79
	473	8.03244×10^{-7}	0.80312	1.21766×10^{-10}	99.97
	498	1.54239×10^{-6}	0.78141	3.39004×10^{-11}	99.61
	523	3.59935×10^{-6}	0.71735	5.27364×10^{-11}	99.87
	548	6.04217×10^{-6}	0.6386	4.95918×10^{-11}	99.76
	573	1.23803×10^{-5}	0.62052	1.37628×10^{-9}	99.76
	598	1.96096×10^{-5}	0.58037	6.44253×10^{-9}	99.77
	623	3.43429×10^{-5}	0.53655	1.26383×10^{-9}	99.89
	648	4.88389×10^{-5}	0.49457	1.04103×10^{-10}	99.65

sites is determined by this increasing tendency of the conductivity with temperature.[80] Furthermore, when the temperature rises, so does the mobility of charge carriers in the sample, as well as the number of transit sites available, allowing the charge carrier to go from one transit site to the next without acquiring much energy.[81] The hopping frequency is the frequency at which dispersion occurs in general, and it tends toward higher-frequency regions as the temperature rises. This behavior shows that the material contains a hopping-type electrical conduction mechanism determined by Jonscher's power law.[52,81] According to Jonscher, the relaxation phenomenon caused by moveable charge carriers is the origin of frequency-dependent ac conductivity. When charge carriers hop from one position to another, they stay in motion between the two potential energy minima. Jonscher's power law states that the relaxation is caused by the mobile charge carriers when transiting from the initial state of minimum potential energy to a new site, which is a state between two potential energy minima. Jonscher's universal power law is a comprehensive analysis of the material's ac conductivity,[81] which is given by

$$\sigma(\omega) = \sigma_{dc} + A\omega^n \tag{8}$$

where σ denotes the total electrical conductivity, σ_{dc} is the dc conductivity, and A denotes the temperature-dependent constant that estimates the polarizability strength, whereas n is interpreted as the frequency exponent depending both on the temperature and frequency and $0 \leq n \leq 1$. It refers to how

much the mobile charge interacts with the surrounding lattices. The fitting results are summarized in Table 2.

The exponent "n" specifies the degree of contact between the lattice and mobile ions, and its variations with the temperature and frequency reflect the kind of conduction mechanism occurring in the substance. To identify the conductivity's conduction method, various theoretical models such as correlated barrier hopping (CBH), quantum mechanical tunneling (QMT), nonoverlapping small polaron tunneling (SPT), and overlapping long polaron tunneling (OLPT) are explored.[82] The QMT model posits that above the Coulomb barrier, the charge carriers hop between two sites, and the exponent n values drop with increasing temperature. It is premised on phonon-assisted electron tunneling and estimates a small rise in n with rising temperature or an independent rise with rising temperature. The SPT model anticipates that n will increase monotonously as the temperature rises, but the OLPT model estimates that n will drop as the temperature rises until a specific point and then increase as the temperature rises further. In the case of CBH, however, as the temperature rises, "n" decreases. The slope of the line in the high-frequency dispersion area in Figure 14a−c may be used to estimate the value of n at a given temperature. From Table 2, it appears that when the temperature rises, the values of n for all samples reduce. This endorses the CBH model's claim that the conduction mechanism of conductivity in the current samples is correlated.[53] Employing this approach, the ac conductivity may be estimated as follows:
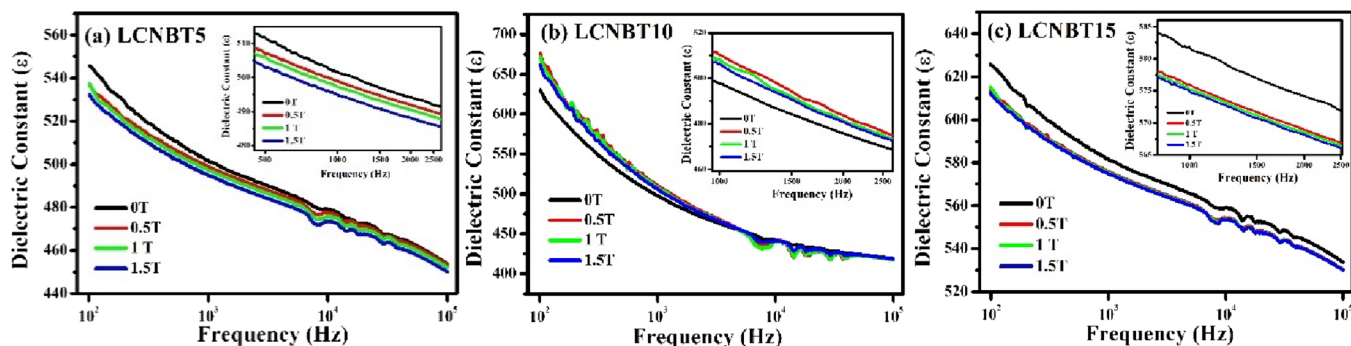
Figure 15. Frequency-dependent behavior of dielectric permittivity (ε) of (a) LCNBT5, (b) LCNBT10, and (c) LCNBT15 at static magnetic fields of 0, 0.5, 1, and 1.5 T. Insets show the zoomed-in view for a particular range of frequencies.

$$\sigma(\omega) = \frac{1}{24}\pi^3 N^2 \varepsilon \varepsilon_0 \omega R_\omega^6 \qquad (9)$$

where N^2 is proportional to the square of the density of the states and R_ω signifies the frequency hopping distance and may be written as

$$R_\omega = \frac{e^2}{\pi\varepsilon\varepsilon_0[W_M + K_B T \ln(\omega\tau_0)]} \qquad (10)$$

$$W_m = W_M - \frac{ne^2}{\pi\varepsilon\varepsilon_0 R_\omega} \qquad (11)$$

where τ_0 denotes the typical relaxation time in the order of an atom's vibrational period ($\approx 10^{-13}$ s), K_B represents Boltzmann's constant, and W_M denotes the maximum barrier height at infinite separation, i.e., the energy required to move the electron from a site to infinity. The Coulomb wells overlap for adjacent sites separated by R_ω and result in a lowering of the effective barrier height from W_M to W_m, as shown in eq 11, and "n" represents the number of electrons involved in a hop ($n = 1$ and $n = 2$ for the single polaron and bipolaron processes, respectively).[83]

The inset of Figure 14a–c shows the change of the logarithmic value of dc conductivity with the reciprocal of the absolute temperature of the investigated compounds LCNBT5, LCNBT10, and LCNBT15 across a broad frequency range. The ac conductivity increases with temperature rise and varies linearly with temperature, exhibiting a negative temperature coefficient of resistance (NTCR) behavior. The Arrhenius equation is used to calculate the activation energy in a thermally activated process:[84]

$$\sigma_{dc} = \sigma_0 \exp\left(-\frac{E_a}{k_B T}\right) \qquad (12)$$

where σ_0 represents the pre-exponential factor also known as conductivity at ambient temperature, T denotes the absolute temperature, and k_B is the Boltzmann constant. This activation energy can be calculated using the slope of linearly fitted curves, and it is required to transform a bound charge carrier into a moveable one capable of participating in the conduction phenomenon. The dc activation energy E_a is estimated using the slope of the linear fit of the $\ln(\sigma_{dc})$ vs $10^3 T^{-1}$ curve and is estimated to be 0.5, 0.64, and 0.69 eV for LCNBT5, LCNBT10, and LCNBT15, respectively.

The entrapment of ions around doubly ionized oxygen vacancies may generate dielectric relaxation in ac conductivity, and the electrical properties of LCNBT ceramics are directly

linked to oxygen defects.[85] These oxygen vacancies might easily be created by an oxygen loss from the crystal lattice at low oxygen partial pressures during high-temperature sintering. Consequently, excess electrons and oxygen vacancies are generated, which may be represented in Kroger–Vink notation[86] as

$$O_o \rightarrow \frac{1}{2}O_2 + V_o \qquad (13a)$$

$$V_o \rightarrow V_o^\blacksquare + e' \qquad (13b)$$

$$V_o \leftrightarrow V_o^{\blacksquare\blacksquare} + e'' \qquad (13c)$$

$$O_o \rightarrow \frac{1}{2}O_2 + V_o^{\blacksquare\blacksquare} + 2e \qquad (14)$$

As demonstrated in eqs 13a and 13b, the electrons created during the generation of oxygen vacancies can establish bonds with Ti^{4+} and Co^{3+} ions, and thermal activation of the trapped electrons by these ions or oxygen vacancies can enhance conduction.

$$Ti^{4+} + e \leftrightarrow Ti^{3+} \qquad (15a)$$

$$Co^{3+} + e \leftrightarrow Co^{2+} \qquad (15b)$$

In perovskite materials, doubly charged oxygen vacancies are thought to be the most mobile charges, and they play a key part in the conduction process.[87] As a result of the activation energies obtained from impedance, modulus, and ac conductivity, it appears that doubly ionized oxygen vacancies may assist ionic charge carrier conduction.

3.5. Magnetodielectric Properties. Under the impact of a magnetic field, the modification of capacitance/dielectric permittivity gives sufficient parameters for multifunctional device applications. The magnetoelectric (ME) coupling permits us to tune magnetization (M) by the application of an electric field (E) or to change electrical polarization (P) with the help of the magnetic field (H). The magnetodielectric response (MDR) may be used to analyze ME coupling behavior.[32]

The frequency-dependent dielectric measurements in the presence and absence of a magnetic field for LCNBT5, LCNBT10, and LCNBT15 samples at 0, 0.5, 1, and 1.5 T fields were carried out to investigate room-temperature magnetodielectric response. Figure 15a–c depicts the dielectric constant (ε') vs frequency plots generated at room temperature for LCNBT5, LCNBT10, and LCNBT15 samples. The findings clearly show that ε' is larger in the absence of a
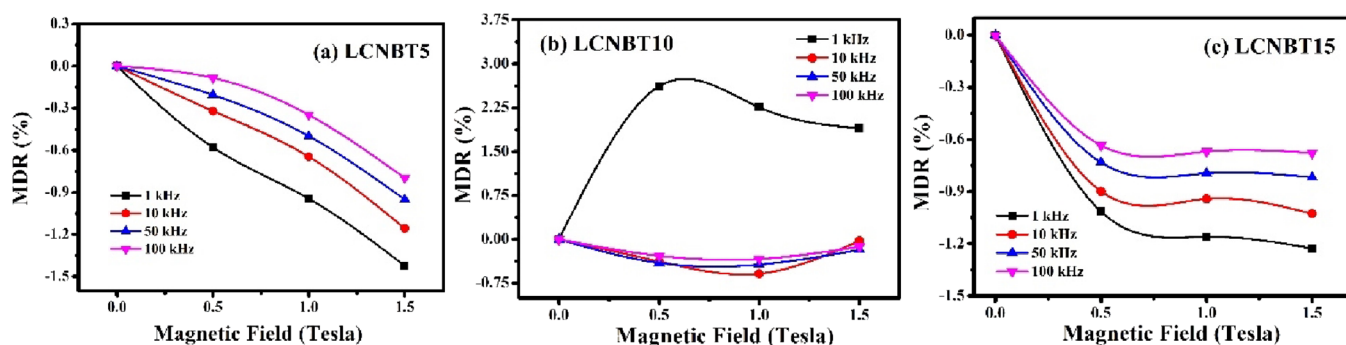
Figure 16. MDR variation at different magnetic fields (0.5, 1, and 1.5 T) and different frequencies for (a) LCNBT5, (b) LCNBT10, and (c) LCNBT15 samples.

magnetic field for LCNBT5 and LCNBT15 samples, but it lowers mainly at low frequencies in the presence of a magnetic field. Furthermore, for all of the applied magnetic fields, it shows no significant change in ε'. The drop in ε' in our samples at low frequencies might be attributable to a shift in space charge polarization produced by the applied magnetic field.[31] Dielectric permittivity, on the other hand, rises only at low frequencies in the presence of a magnetic field for the LCNBT10 sample. The data clearly show that for all samples, for a given magnetic field, ε' declines with an increasing frequency. The simultaneous existence of electric and magnetic domains in multiferroic materials is thought to be the source of magnetoelectric interaction. The material is strained as a result of the application of a magnetic field, and this generated strain causes stress in the material, which causes an electric field to form in the sample. As a result, the materials' dielectric properties are altered.[88]

Negative MDR is defined as a decrease in a magnetic field at a specific frequency. With the introduction of a magnetic field, the drop in ε' for LCNBT5 and LCNBT15 samples indicates that these samples have a negative magnetodielectric response. However, the LCNBT10 sample shows a positive magnetodielectric response at 1 kHz. The spin pair correlations of neighboring spins and the coupling constant determine the negative value of ME coupling behavior.[32] This decrement may often be because of several factors such as magnetoelectric coupling, magnetostriction effect, or magnetoresistance.[89] The magnetodielectric coupling may be quantified using the magnetodielectric response (MDR %), which is estimated with the help of the relation[90] given below:

$$\text{MDR}\,(\%) = \frac{\varepsilon'(H) - \varepsilon'(0)}{\varepsilon'(0)} \times 100\% \tag{16}$$

where $\varepsilon'(H)$ and $\varepsilon'(0)$ indicate the dielectric constant in the presence of a magnetic field and in the absence of one, respectively.[31] Figure 16a−c displays the MDR variation with respect to the applied magnetic field at particular frequencies for LCNBT5, LCNBT10, and LCNBT15 samples, and it can be seen that all of the samples exhibit a negative magnetodielectric response, except for LCNBT10 at 1 kHz at all the applied fields. The samples' space charge polarization might be the cause of the negative MDR.

4. CONCLUSIONS

By employing the sol−gel method and calcination/sintering temperatures of 850 and 1000 °C, respectively, polycrystalline samples of LaCoO$_3$-doped NBT with varying concentrations of

x = 0.05, 0.10, and 0.15 were successfully prepared. Dielectric studies show that the dielectric constant increases with temperature due to increased charge carrier mobility, leading to enhanced space charge polarization and conductivity. Two dielectric anomalies, a frequency-dispersive shoulder at a lower temperature (T_s) ranging from 425 to 450 K, which is associated with polar nanoregions (PNRs), and the Curie temperature (T_c) transition from a ferroelectric to paraelectric state, ranging from 580 to 650 K, were observed in LCNBT samples. The modified Curie−Weiss law was employed to determine the order of diffusivity or disorderliness in the prepared samples. The calculated values for LCNBT5, LCNBT10, and LCNBT15 at 100 kHz were 1.73, 2.03, and 1.69, respectively, indicating that the phase transition in NBT is a diffuse phase transition (DPT). At higher frequencies, the dielectric constant decreases due to electron exchange between Co^{2+} and Co^{3+} ions and Ti^{3+} and Ti^{4+} ions at the octahedral site. At low frequencies and high temperatures, the substantial dielectric constant value can be explained by the Maxwell−Wagner model and Koop's two-layer model. The impedance spectra show well-defined broad and asymmetric relaxation peaks with a wide range of relaxation durations, indicating non-Debye-type behavior, which is corroborated by modulus spectroscopy and conductivity analysis, aiding in understanding the transport phenomena. The ac conductivity spectrum is governed by Jonscher's universal power law, and the decreasing value of the conductivity exponent "n" as the temperature rises suggests that the correlated barrier hopping (CBH) model may adequately describe the electrical conduction process. Doubly ionized oxygen ion vacancies are responsible for the relaxation and conduction processes in ceramics. All samples exhibit a negative magnetodielectric response (MDR), i.e., ε' decreases with an increase in frequency for a given magnetic field, except for LCNBT10 at 1 kHz.

■ ASSOCIATED CONTENT

ⓢ Supporting Information

The Supporting Information is available free of charge at https://pubs.acs.org/doi/10.1021/acsomega.3c04490.

> FESEM micrographs; grain size distribution; experimental, theoretical, and relative density; high-resolution XPS spectra of Ti 2p and Co 2p (PDF)

■ AUTHOR INFORMATION

Corresponding Authors

Surinder Singh − *Department of Physics, Guru Nanak Dev University, Amritsar 143005 Punjab, India;* ● orcid.org/0000-0002-8642-0828; Email: surinderphy.rsh@gndu.ac.in

Lakhwant Singh − *Department of Physics, Guru Nanak Dev University, Amritsar 143005 Punjab, India;* Email: lakhwant@yahoo.com

Authors

Anumeet Kaur − *Department of Physics, Guru Nanak Dev University, Amritsar 143005 Punjab, India; Department of Applied Sciences and Humanities, Global Group of Institutes, Amritsar 143501 Punjab, India;* ● orcid.org/0000-0002-6147-4715

Parwinder Kaur − *Department of Physics, Guru Nanak Dev University, Amritsar 143005 Punjab, India*

Complete contact information is available at:
https://pubs.acs.org/10.1021/acsomega.3c04490

Notes

The authors declare no competing financial interest.

■ REFERENCES

(1) Hu, B.; Fan, H.; Ning, L.; Gao, S.; Yao, Z.; Li, Q. Enhanced Energy-Storage Performance and Dielectric Temperature Stability of $(1-x)(0.65Bi_{0.5}Na_{0.5}TiO_3-0.35Bi_{0.1}Sr_{0.85}TiO_3)$-XKNbO$_3$ Ceramics. *Ceram. Int.* **2018**, *44*, 10968−10974.

(2) Yan, B.; Fan, H.; Wang, C.; Zhang, M.; Yadav, A. K.; Zheng, X.; Wang, H.; Du, Z. Giant Electro-Strain and Enhanced Energy Storage Performance of $(Y_{0.5}Ta_{0.5})^{4+}$ Co-Doped $0.94(Bi_{0.5}Na_{0.5})TiO_3$-$0.06BaTiO_3$ Lead-Free Ceramics. *Ceram. Int.* **2020**, *46*, 281−288.

(3) Whittingham, M. S. Materials Challenges Facing Electrical Energy Storage. *MRS Bull.* **2008**, *33*, 411−419.

(4) Yang, L.; Kong, X.; Li, F.; Hao, H.; Cheng, Z.; Liu, H.; Li, J. F.; Zhang, S. Perovskite Lead-Free Dielectrics for Energy Storage Applications. *Prog. Mater. Sci.* **2019**, *102*, 72−108.

(5) Wan, T.; Zhang, L.; Du, H.; Lin, X.; Qu, B.; Xu, H.; Li, S.; Chu, D. Recent Developments in Oxide-Based Ionic Conductors: Bulk Materials, Nanoionics, and Their Memory Applications. *Crit. Rev. Solid State Mater. Sci.* **2018**, *43*, 47−82.

(6) Palneedi, H.; Peddigari, M.; Hwang, G. T.; Jeong, D. Y.; Ryu, J. High-Performance Dielectric Ceramic Films for Energy Storage Capacitors: Progress and Outlook. *Adv. Funct. Mater.* **2018**, *28*, 1−33.

(7) Zhou, W.; Deng, H.; Yang, P.; Chu, J. Structural Phase Transition, Narrow Band Gap, and Room-Temperature Ferromagnetism in $[KNbO_3]_{1-x}[BaNi_{1/2}Nb_{1/2}O_{3-\delta}]_x$ ferroelectrics. *Appl. Phys. Lett.* **2014**, *105*, 1−5.

(8) Shi, T.; Li, G.; Zhu, J. Compositional Design Strategy for High Performance Ferroelectric Oxides with Perovskite Structure. *Ceram. Int.* **2017**, *43*, 2910−2917.

(9) Choi, T.; Lee, S.; Choi, Y. J.; Kiryukhin, V.; Cheong, S.-W. Switchable Ferroelectric Diode and Photovoltaic Effect in BiFeO$_3$. **2009**, *324* (5923), 63−66. DOI: 10.1126/science.1168636.

(10) Long, C.; Li, T.; Fan, H.; Wu, Y.; Zhou, L.; Li, Y.; Xiao, L.; Li, Y. Li-Substituted $K_{0.5}Na_{0.5}NbO_3$-Based Piezoelectric Ceramics: Crystal Structures and the Effect of Atmosphere on Electrical Properties. *J. Alloys Compd.* **2016**, *658*, 839−847.

(11) Fan, P.; Liu, K.; Ma, W.; Tan, H.; Zhang, Q.; Zhang, L.; Zhou, C.; Salamon, D.; Zhang, S. T.; Zhang, Y.; Nan, B.; Zhang, H. Progress and Perspective of High Strain NBT-Based Lead-Free Piezoceramics and Multilayer Actuators. *J. Mater.* **2021**, *7*, 508−544.

(12) Zhao, C.; Huang, Y.; Wu, J. Multifunctional Barium Titanate Ceramics via Chemical Modification Tuning Phase Structure. *InfoMat* **2020**, *2*, 1163−1190.

(13) Dong, G.; Fan, H.; Liu, L.; Ren, P.; Cheng, Z.; Zhang, S. Large Electrostrain in $Bi_{1/2}Na_{1/2}TiO_3$-Based Relaxor Ferroelectrics: A Case Study of $Bi_{1/2}Na_{1/2}TiO_3$-$Bi_{1/2}K_{1/2}TiO_3$-$Bi(Ni_{2/3}Nb_{1/3})O_3$ Ceramics. *J. Mater.* **2021**, *7*, 593−602.

(14) Grinberg, I.; West, D. V.; Torres, M.; Gou, G.; Stein, D. M.; Wu, L.; Chen, G.; Gallo, E. M.; Akbashev, A. R.; Davies, P. K.; Spanier, J. E.; Rappe, A. M. Perovskite Oxides for Visible-Light-Absorbing Ferroelectric and Photovoltaic Materials. *Nature* **2013**, *503*, 509−512.

(15) Bayart, A.; Szczepanski, F.; Blach, J. F.; Rousseau, J.; Katelnikovas, A.; Saitzek, S. Upconversion Luminescence Properties and Thermal Quenching Mechanisms in the Layered Perovskite $La_{1.9}Er_{0.1}Ti_2O_7$ towards an Application as Optical Temperature Sensor. *J. Alloys Compd.* **2018**, *744*, 516−527.

(16) Singh, S.; Kaur, A.; Kaur, P.; Singh, L. An Investigation on Cubic and Monoclinic Phase Coexistence in Sol-Gel Derived $LaFeO_3$-$Na_{0.5}Bi_{0.5}TiO_3$ Ceramics. *J. Alloys Compd.* **2021**, *857*, No. 158284.

(17) Singh, S.; Kaur, A.; Kaur, P.; Singh, L. Oxygen Vacancies Induced Anomalies in the Structural, Ferroelectric and Magnetic Behaviour of Sol-Gel Derived $LaCoO_3$ Modified $Na_{0.5}Bi_{0.5}TiO_3$ Ceramics. *Mater. Chem. Phys.* **2022**, *279*, No. 125754.

(18) Simon, A.; Ravez, J.; Maglione, M. Relaxor Properties of $Ba_{0.9}Bi_{0.067}(Ti_{1-X}Zr_x)O_3$ Ceramics. *Solid State Sci.* **2005**, *7*, 925−930.

(19) Reichmann, K.; Feteira, A.; Li, M. Bismuth Sodium Titanate Based Materials for Piezoelectric Actuators. *Mater.* **2015**, *8*, 8467−8495.

(20) Aksel, E.; Forrester, J. S.; Jones, J. L.; Thomas, P. A.; Page, K.; Suchomel, M. R. Monoclinic Crystal Structure of Polycrystalline $Na_{0.5}Bi_{0.5}TiO_3$. *Appl. Phys. Lett.* **2011**, *98*, 2009−2012.

(21) Jones, G. O.; Thomas, P. A. The Tetragonal Phase of $Na_{0.5}Bi_{0.5}TiO_3$ ± a New Variant of the Perovskite Structure. *Acta Crystallogr., Sect. B: Struct. Sci.* **2000**, *56*, 426−430.

(22) Gorfman, S.; Glazer, A. M.; Noguchi, Y.; Miyayama, M.; Luo, H.; Thomas, P. A. Observation of a Low-Symmetry Phase in $Na_{0.5}Bi_{0.5}TiO_3$ Crystals by Optical Birefringence Microscopy. *J. Appl. Crystallogr.* **2012**, *45*, 444−452.

(23) Rao, B. N.; Olivi, L.; Sathe, V.; Ranjan, R. Electric Field and Temperature Dependence of the Local Structural Disorder in the Lead-Free Ferroelectric N $A_{0.5}$ B $I_{0.5}$Ti O$_3$: An EXAFS Study. *Phys. Rev. B* **2016**, *93*, 1−10.

(24) Cai, L.; Toulouse, J.; Luo, H.; Tian, W. Anisotropic Phonon Coupling in the Relaxor Ferroelectric $(Na_{1/2} Bi_{1/2}) TiO_3$ near Its High-Temperature Phase Transition. *Phys. Rev. B: Condens. Matter Mater. Phys.* **2014**, *90*, 1−9.

(25) Shi, J.; Liu, X.; Tian, W. Structure Evolution and Ferroelectric Properties in Stoichiometric $Bi_{0.5+x}Na_{0.5-x}Ti_{1-0.5}xO_3$. *J. Mater. Sci.* **2019**, *54*, 5249−5255.

(26) He, X.; Mo, Y. Accelerated Materials Design of $Na_{0.5}Bi_{0.5}TiO_3$ Oxygen Ionic Conductors Based on First Principles Calculations. *Phys. Chem. Chem. Phys.* **2015**, *17*, 18035−18044.

(27) Dawson, J. A.; Chen, H.; Tanaka, I. Crystal Structure, Defect Chemistry and Oxygen Ion Transport of the Ferroelectric Perovskite, $Na_{0.5}Bi_{0.5}TiO_3$: Insights from First-Principles Calculations. *J. Mater. Chem. A* **2015**, *3*, 16574−16582.

(28) Yang, F.; Li, M.; Li, L.; Wu, P.; Pradal-Velázquez, E.; Sinclair, D. C. Defect Chemistry and Electrical Properties of Sodium Bismuth Titanate Perovskite. *J. Mater. Chem. A* **2018**, *6*, 5243−5254.

(29) Li, M.; Zhang, H.; Cook, S. N.; Li, L.; Kilner, J. A.; Reaney, I. M.; Sinclair, D. C. Dramatic Influence of A-Site Nonstoichiometry on the Electrical Conductivity and Conduction Mechanisms in the Perovskite Oxide $Na_{0.5}Bi_{0.5}TiO_3$. *Chem. Mater.* **2015**, *27*, 629−634.

(30) Nandy, S.; Mocherla, P. S. V.; Abdelhamid, E.; Nadgorny, B.; Naik, R.; Sudakar, C. Coexistence of Large Negative and Positive Magnetodielectric Response in $Bi_{1-X}CaxFe_{1-Y}Tiy$ $O_{3-\delta}$ Nanoparticle Ceramics. *Phys. Rev. B* 2021, *103*, 1−8.

(31) Catalan, G. Magnetocapacitance without Magnetoelectric Coupling. *Appl. Phys. Lett.* 2006, *88*, 1−4.

(32) Pradhan, D. K.; Puli, V. S.; Narayan Tripathy, S.; Pradhan, D. K.; Scott, J. F.; Katiyar, R. S. Room Temperature Multiferroic Properties of $Pb(Fe_{0.5}Nb_{0.5})O_3-Co_{0.65}Zn_{0.35}Fe_2O_4$ Composites. *J. Appl. Phys.* 2013, *114*, 234106.

(33) Rahman, M. A.; Hossain, A. K. M. A. Relaxation Mechanism of $(x)Mn_{0.45}Ni_{0.05}Zn_{0.50}Fe_2O_4 + (1 - X)BaZr_{0.52}Ti_{0.48}O_3$ Multiferroic Materials. *Phys. Scr.* 2014, *89*, No. 115811.

(34) Mathe, V. L.; Kamble, R. B. Anomalies in Electrical and Dielectric Properties of Nanocrystalline Ni-Co Spinel Ferrite. *Mater. Res. Bull.* 2008, *43*, 2160−2165.

(35) Verma, A.; Thakur, O. P.; Prakash, C.; Goel, T. C.; Mendiratta, R. G. Temperature Dependence of Electrical Properties of Nickel-Zinc Ferrites Processed by the Citrate Precursor Technique. *Mater. Sci. Eng., B* 2005, *116*, 1−6.

(36) Gupta, A.; Chatterjee, R. Dielectric and Magnetoelectric Properties of $BaTiO_3-Co_{0.6}Zn_{0.4}Fe_{1.7}Mn_{0.3}O_4$ Composite. *J. Eur. Ceram. Soc.* 2013, *33*, 1017−1022.

(37) Kulkarni, S. R.; Kanamadi, C. M.; Patankar, K. K.; Chougule, B. K. Magnetic Properties and Magnetoelectric Effect in $Ni_{0.8}Co_{0.1}Cu_{0.1}Fe_2O_4 + PbZr_{0.2}Ti_{0.8}O_3$ Composites. *J. Mater. Sci.* 2005, *40*, 5691−5694.

(38) Liu, X.; Zhai, J.; Shen, B. Local Phenomena in Bismuth Sodium Titanate Perovskite Studied by Raman Spectroscopy. *J. Am. Ceram. Soc.* 2018, *101*, 5604−5614.

(39) Parija, B.; Badapanda, T.; Senthil, V.; Rout, S. K.; Panigrahi, S. Diffuse Phase Transition, Piezoelectric and Optical Study of $Bi_{0.5}Na_{0.5}TiO_3$ Ceramic. *Bull. Mater. Sci.* 2012, *35*, 197−202.

(40) Glinchuk, M. D.; Bykov, I. P.; Kornienko, S. M.; Laguta, V. V.; Slipenyuk, A. M.; Bilous, A. G.; V'yunov, O. I.; Yanchevskii, O. Z. Influence of Impurities on the Properties of Rare-Earth-Doped Barium- Titanate Ceramics. *J. Mater. Chem.* 2000, *10*, 941−947.

(41) Choudhary, T. A. R. N. P. Dielectric Behavior of Manganese Titanate in the Paraelectric Phase. *Appl. Phys. A: Mater. Sci. Process.* 2015, *121*, 707−714.

(42) Bammannavar, B. K.; Naik, L. R. Electrical Properties and Magnetoelectric Effect in $(x)Ni_{0.5}Zn_{0.5}Fe_2O_4+(1-x)BPZT$ Composites. *Smart Mater. Struct.* 2009, *18*, No. 085013.

(43) Patankar, K. K.; Joshi, S. S.; Chougule, B. K. Dielectric Behaviour in Magnetoelectric Composites. *Phys. Lett. A* 2005, *346*, 337−341.

(44) Murthy, V. R. K.; Sobhanadri, J. Dielectric Properties of Some Nickel-Zinc Ferrites at Radio Frequency. *Phys. Status Solidi A* 1976, *36*, 133−135.

(45) Koops, C. G. On the Dispersion of Resistivity and Dielectric Constant of Some Semiconductors at Audiofrequencies. *Phys. Rev.* 1951, *83*, 121−124.

(46) Elissalde, C.; Ravez, J. Ferroelectric Ceramics: Defects and Dielectric Relaxations. *J. Mater. Chem.* 2001, *11*, 1957−1967.

(47) Das, S.; Biswal, A. K.; Parida, K.; Choudhary, R. N. P.; Roy, A. Applied Surface Science Electrical and Mechanical Behavior of PMN-PT/CNT Based Polymer Composite Film for Energy Harvesting. *Appl. Surf. Sci.* 2018, *428*, 356−363.

(48) Kharabe, R. G.; Devan, R. S.; Kanamadi, C. M.; Chougule, B. K. Dielectric Properties of Mixed Li-Ni-Cd Ferrites. *Smart Mater. Struct.* 2006, *15*, 1−N39.

(49) Das, R.; Choudhary, R. N. P. Studies of Structural , Dielectric Relaxor and Electrical Characteristics of Lead- Free Double Perovskite : Gd_2NiMnO_6. *Solid State Sci.* 2019, *87*, 1−8.

(50) Jonscher, A. K. Dielectric Relaxation in Solids. *J. Phys. D: Appl. Phys.* 1999, *32*, R57.

(51) Khalil, R. Impedance and Modulus Spectroscopy of Poly(Vinyl Alcohol)-$Mg[ClO_4]_2$ Salt Hybrid Films. *Appl. Phys. A: Mater. Sci. Process.* 2017, *123*, 1−7.

(52) Sinclair, D. C.; West, A. R. Impedance and Modulus Spectroscopy of Semiconducting $BaTiO_3$ Showing Positive Temperature Coefficient of Resistance. *J. Appl. Phys.* 1989, *66*, 3850−3856.

(53) Abdelrazek, E. M.; Abdelghany, A. M.; Tarabiah, A. E.; Zidan, H. M. AC Conductivity and Dielectric Characteristics of PVA/PVP Nanocomposite Filled with MWCNTs. *J. Mater. Sci.: Mater. Electron.* 2019, *30*, 15521−15533.

(54) Irvine, B. J. T. S.; Sinclair, D. C.; West, A. R. Electroceramics Characterisation by Impedance Sepctroscopy.Pdf. *Arch. Fr. Pediatr.* 1985, *42*, 575−576.

(55) Mizaras, R.; Takashige, M.; Banys, J.; Kojima, S.; Grigas, J.; Hamazaki, S. I.; Brilingas, A. Dielectric Relaxation in $Ba_2NaNb_5(1-x)Ta_5xO_{15}$ Single Crystals. *J. Phys. Soc. Jpn.* 1997, *66*, 2881−2885.

(56) James, A. R.; Srinivas, K. Low Temperature Fabrication and Impedance Spectroscopy of PMN-PT Ceramics. *Mater. Res. Bull.* 1999, *34*, 1301−1310.

(57) Zheng, Q.; Fan, H.; Long, C. Microstructures and Electrical Responses of Pure and Chromium-Doped $CaCu3Ti4O12$ Ceramics. *J. Alloys Compd.* 2012, *511*, 90−94.

(58) Zubair, M. A.; Mozahid, F. A.; Takeda, H.; Hossain, A. K. M. A. Effect of Processing Temperature on Structural, Optical and Frequency Dependent Electrical Responses of Solid-State Sintered Bismuth Sodium Titanate. *Mater. Sci. Eng., B* 2021, *274*, No. 115474.

(59) James, A. R.; Priya, S.; Uchino, K.; Srinivas, K. Dielectric Spectroscopy of $Pb(Mg_{1/3}Nb_{2/3})O_3-PbTiO_3$ Single Crystals. *J. Appl. Phys.* 2001, *90*, 3504−3508.

(60) Chandra, K. P.; Prasad, K.; Gupta, R. N. Impedance Spectroscopy Study of an Organic Semiconductor: Alizarin. *Phys. B* 2007, *388*, 118−123.

(61) Tirupathi, P.; Kumar, N.; Pastor, M.; Pandey, A. C.; Choudhary, R. N. P. Diffused Phase Transitions in $Pb(Zr_{0.65}Ti_{0.35})O_3-Pb(Fe_{2/3}W_{1/3})O_3$ Multiferroics. *J. Appl. Phys.* 2015, *117*, 8.

(62) Pastor, M.; Kumar, N.; Kumar, B.; Panwar, K.; Biswas, K.; Pandey, A. C. Study of Diffuse Phase Transition in $Pb(Cd_{1/3}Nb_{2/3})O_3$ Compound. *J. Alloys Compd.* 2014, *615*, 40−46.

(63) Bhasin, T.; Agarwal, A.; Sanghi, S.; Kotnala, R. K.; Shah, J.; Yadav, M.; Tuteja, M.; Singh, J. Crystal Structure, Dielectric, Magnetic and Improved Magnetoelectric Properties of $XNiFe_2O_4$-$(1-x)Na_{0.5}Bi_{0.5}TiO_3$ Composites. *Mater. Res. Express* 2018, *5*, 0−15.

(64) Purohit, V.; Padhee, R.; Choudhary, R. N. P. Dielectric and Impedance Spectroscopy of $Bi(Ca_{0.5}Ti_{0.5})O_3$ Ceramic. *Ceram. Int.* 2018, *44*, 3993−3999.

(65) Sahoo, S.; Mahapatra, P. K.; Choudhary, R. N. P. The Structural, Electrical and Magnetoelectric Properties of Soft-Chemically-Synthesized $SmFeO3$ Ceramics. *J. Phys. D: Appl. Phys.* 2016, *49*, No. 035302.

(66) Gupta, P.; Padhee, R.; Mahapatra, P. K.; Choudhary, R. N. P.; Das, S. Structural and Electrical Properties of Bi_3TiVO_9 Ferroelectric Ceramics. *J. Alloys Compd.* 2018, *731*, 1171−1180.

(67) Mujasam Batoo, K. Study of Dielectric and Impedance Properties of Mn Ferrites. *Phys. B* 2011, *406*, 382−387.

(68) Ragoisha, G. A.; Bondarenko, A. S. Potentiodynamic Electrochemical Impedance Spectroscopy. *Electrochim. Acta* 2005, *50*, 1553−1563.

(69) Martiren, H. T.; Burfoot, J. C. Grain-Size and Pressure Effects on the Dielectric and Piezoelectric Properties of Hot-Pressed PZT-5. *Ferroelectrics* 1974, *7*, 151−152.

(70) Hajra, S.; Sahoo, S.; Das, R.; Choudhary, R. N. P. Structural, Dielectric and Impedance Characteristics of $(Bi_{0.5}Na_{0.5})TiO_3-BaTiO_3$ Electronic System. *J. Alloys Compd.* 2018, *750*, 507−514.

(71) Sakthisabarimoorthi, A.; Martin Britto Dhas, S. A.; Robert, R.; Jose, M. Influence of Erbium Doping on the Electrical Behaviour of $CaCu_3Ti_4O_{12}$ Ceramics Probed by Impedance Spectroscopy Analysis. *Mater. Res. Bull.* 2018, *106*, 81−92.

(72) Zangina, T.; Hassan, J.; Matori, K. A.; Azis, R. S.; Ahmadu, U.; See, A. Sintering Behavior, Ac Conductivity and Dielectric Relaxation of $Li_{1.3}Ti_{1.7}Al_{0.3}(PO_4)_3$ NASICON Compound. *Results Phys.* 2016, *6*, 719−725.

(73) El-Falaky, G. E.; Guirguis, O. W.; Abd El-Aal, N. S. A.C. Conductivity and Relaxation Dynamics in Zinc−Borate Glasses. *Prog. Nat. Sci.: Mater. Int.* **2012**, *22*, 86−93.

(74) Isasi, J.; López, M. L.; Veiga, M. L.; Ruiz-Hitzky, E.; Pico, C. Structural Characterization and Electrical Properties of a Novel Defect Pyrochlore. *J. Solid State Chem.* **1995**, *116*, 290−295.

(75) Hodge, I. M.; Ingram, M. D.; West, A. R. Impedance and Modulus Spectroscopy of Polycrystalline Solid Electrolytes. *J. Electroanal. Chem.* **1976**, *74*, 125−143.

(76) Singh, S.; Kaur, A.; Kaur, P.; Singh, L. Unveiling the High-Temperature Dielectric Relaxation and Conduction Mechanisms in Sol-Gel Derived $LaFeO_3$ Modified Sodium Bismuth Titanate Ceramics. *J. Alloys Compd.* **2023**, *941*, No. 169023.

(77) Bergman, R. General Susceptibility Functions for Relaxations in Disordered Systems. *J. Appl. Phys.* **2000**, *88*, 1356−1365.

(78) Agrawal, L.; Singh, B. P.; Sinha, T. P. Dielectric Relaxation in Complex Perovskite Oxide $In(Ni_{1/2}Zr_{1/2})O_3$. *Mater. Res. Bull.* **2009**, *44*, 1858−1862.

(79) Hemalatha, K. S.; Sriprakash, G.; Ambika Prasad, M. V. N.; Damle, R.; Rukmani, K. Temperature Dependent Dielectric and Conductivity Studies of Polyvinyl Alcohol-ZnO Nanocomposite Films by Impedance Spectroscopy. *J. Appl. Phys.* **2015**, *118*, 154103.

(80) Pollak, M.; Geballe, T. H. Low-Frequency Conductivity Due to Hopping Processes in Silicon. *Phys. Rev.* **1961**, *122*, 1742−1753.

(81) Jonscher, A. K. The Universal Dielectric Response. *Nat.* **1977**, *267*, 673−679.

(82) Sassi, M.; Bettaibi, A.; Oueslati, A.; Khirouni, K.; Gargouri, M. Electrical Conduction Mechanism and Transport Properties of $LiCrP2O_7$ Compound. *J. Alloys Compd.* **2015**, *649*, 642−648.

(83) Sharma, A.; Mehta, N. Study of Dielectric Relaxation and Thermally Activated a.c. Conduction in Lead Containing Topological Glassy Semiconductors. *RSC Adv.* **2017**, *7*, 19085−19097.

(84) Halder, S.; Parida, K.; Das, S. N.; Pradhan, S. K.; Bhuyan, S.; Choudhary, R. N. P. Dielectric and Impedance Properties of $Bi(Zn_{2/3}V_{1/3})O_3$ Electronic Material. *Phys. Lett. A* **2018**, *382*, 716−722.

(85) Fei Liu, S.; Li, J.; Ming Chen, X. Effects of Oxygen Vacancies on Dielectric, Electrical, and Ferroelectric Properties of $Ba_4Nd_2Fe_2Nb_8O$ 30 Ceramics. *Appl. Phys. Lett.* **2014**, *104*, 5.

(86) Liu, L.; Huang, Y.; Su, C.; Fang, L.; Wu, M.; Hu, C.; Fan, H. Space-Charge Relaxation and Electrical Conduction in $K_{0.5}Na_{0.5}NbO_3$ at High Temperatures. *Appl. Phys. A: Mater. Sci. Process.* **2011**, *104*, 1047−1051.

(87) Suchanicz, J.; Kluczewska-chmielarz, K.; Sitko, D.; Jag, G. Ł. O. J. Suchanicz. 2021, *10* (1), 152−165.

(88) Palkar, V. R.; Kundaliya, D. C.; Malik, S. K.; Bhattacharya, S. Magnetoelectricity at Room Temperature in the $Bi_{0.9}$-XTb $_xFeO_3$ System. *Phys. Rev. B: Condens. Matter Mater. Phys.* **2004**, *69*, 9−11.

(89) Smit, J.; Wijn, H. P. J. Physical Properties of Ferrites. *Adv. Electron. Electron Phys.* **1954**, *6*, 69−136.

(90) Uniyal, P.; Yadav, K. L. Pr Doped Bismuth Ferrite Ceramics with Enhanced Multiferroic Properties. *J. Phys.: Condens. Matter* **2009**, *21*, No. 405901.